

## Characterization of octupole-type structures in $^{221}\text{Th}$

W. Reviol,<sup>1</sup> R. V. F. Janssens,<sup>2</sup> S. Frauendorf,<sup>3</sup> D. G. Sarantites,<sup>1</sup> M. P. Carpenter,<sup>2</sup> X. Chen,<sup>1,\*</sup> C. J. Chiara,<sup>2,4</sup> D. J. Hartley,<sup>5</sup> K. Hauschild,<sup>6</sup> T. Lauritsen,<sup>2</sup> A. Lopez-Martens,<sup>6</sup> M. Montero,<sup>1,†</sup> O. L. Pechenaya,<sup>7,‡</sup> D. Seweryniak,<sup>2</sup> J. B. Snyder,<sup>7,§</sup> and S. Zhu<sup>2</sup>

<sup>1</sup>*Department of Chemistry, Washington University, St. Louis, Missouri 63130, USA*

<sup>2</sup>*Physics Division, Argonne National Laboratory, Argonne, Illinois 60439, USA*

<sup>3</sup>*Department of Physics, University of Notre Dame, Notre Dame, Indiana 46556, USA*

<sup>4</sup>*Department of Chemistry and Biochemistry, University of Maryland, College Park, Maryland 20742, USA*

<sup>5</sup>*Department of Physics, U.S. Naval Academy, Annapolis, Maryland 21402, USA*

<sup>6</sup>*CSNSM, IN2P3-CNRS, F-91405 Orsay Campus, France*

<sup>7</sup>*Department of Physics, Washington University, St. Louis, Missouri 63130, USA*

(Received 15 July 2014; revised manuscript received 11 September 2014; published 21 October 2014)

A detailed level scheme for  $^{221}\text{Th}$  has been established in an experiment using the  $^{18}\text{O} + ^{207}\text{Pb}$  reaction at 96 MeV. The evaporation residues from this fissile system were selected with the HERCULES detector array and residue-gated  $\gamma$  rays were measured with Gammasphere. Three band structures of interlinked, alternating-parity levels are observed, two of which are non-yrast. In addition, several high-lying excitations are found. The yrast band is seen up to spin-parity  $37/2^-$  and  $39/2^+$ , beyond which a high-spin feeding transition is observed. The non-yrast sequences are interpreted as parity-doublet structures, based on a configuration similar to that of the yrast band in  $^{223}\text{Th}$  ( $K = 5/2$ ). The key properties of even-odd nuclei in this mass region [ $B(E1)/B(E2)$  and  $B(M1)/B(E2)$  ratios, spin alignments, parity splittings] are reviewed.

DOI: [10.1103/PhysRevC.90.044318](https://doi.org/10.1103/PhysRevC.90.044318)

PACS number(s): 27.80.+w, 27.90.+b, 23.20.Lv, 21.60.Ev

### I. INTRODUCTION

In the actinide region, quadrupole-octupole collectivity has a large impact on nuclear structure at low and high spin [1]. A characteristic signature of this collective mode is the appearance of alternating-parity level sequences with strong connecting electric-dipole ( $E1$ ) transitions and bypassing electric-quadrupole ( $E2$ )  $\gamma$  rays. The  $B(E1)/B(E2)$  ratios of transition probabilities are of the order of  $10^{-6}\text{fm}^{-2}$ , which is a benchmark for sequences associated with octupole excitations across the region. For the lighter systems,  $^{224}\text{Th}$ , with neutron number  $N = 134$ , can be viewed as the central nucleus: it is representative of the rotational mode of octupole collectivity, where the level spacing associated with  $E2$  transitions increases with spin. Mean-field calculations for nuclei like  $^{224}\text{Th}$  imply a nuclear shape with static quadrupole and octupole deformations [1]. Among the heavier actinide nuclei, the  $N = 144, 146$  systems  $^{238,240}\text{Pu}$  [2,3] and  $^{238}\text{U}$  [4,5] may be regarded as typical cases for quadrupole-octupole collectivity. Their band structures are examples of octupole surface vibrations superimposed on a quadrupole shape.

Some of the recent experimental work on octupole nuclei has concentrated on the lower border of the region. Here, the

onset of quadrupole-octupole collectivity, just above magic number  $N = 126$ , has been studied in the  $N = 129, 130$  systems  $^{219}\text{Th}$  [6] and  $^{220}\text{Th}$  [7]. The multiple, alternating-parity sequences found in these nuclei match the pattern of benchmark  $B(E1)/B(E2)$  ratios introduced above. However, the levels of the yrast octupole sequence of  $^{220}\text{Th}$ , in particular, show an approximately constant spacing over a large spin range, resembling a vibrational behavior. The observations have been explained, within a phonon picture, by a reflection-asymmetric tidal wave moving over the nuclear surface [7–9]. A related phonon picture has been used to understand the results of the most recent spectroscopic study of  $^{240}\text{Pu}$  [3] and  $^{238}\text{U}$  [5] in terms of the condensation of octupole phonons [10], an alternative to the notion of static quadrupole and octupole deformations. Here,  $^{221}\text{Th}$  and its neighbors will be discussed in terms of both static and dynamic octupole correlations.

For the following, it is useful to review some symmetry aspects of rotating reflection asymmetric nuclei and their implications for the level scheme [1,11]. It is assumed that the nucleus has two reflection planes perpendicular to each other. If the rotational axis is perpendicular to one of these planes, the simplex  $s$  is a good quantum number, and it combines parity  $p$  and spin  $I$  of a given state as  $s = p \exp(i\pi I)$ . For half-integer spins,  $s = \pm i$ . If the angular momentum is not perpendicular to the reflection plane,  $s$  is not a good quantum number and two alternating-parity level sequences arrange themselves into parity doublets. These correspond to pairs of states nearly degenerate in energy with the same spin, but opposite parity. Indeed, the unpaired nucleon may carry a significant angular-momentum component within one of the reflection planes to generate parity doublets. The latter component is the  $K$  quantum number in the case of axial symmetry. For simplicity,  $K$  is used in the following

\*Present address: Department of Radiation Oncology, Medical College of Wisconsin, Milwaukee, WI 53226, USA.

†Present address: Department of Physics, Stanford University, Stanford, CA 94305, USA.

‡Present address: Department of Radiation Oncology, Washington University School of Medicine, St. Louis, MO 63130, USA.

§Present address: Naval Nuclear Power Training Command, Goose Creek, SC 29445, USA.

discussions, although it is not demonstrated that the shape is axial. For a nonaxial shape, it should be taken as a measure of the angular momentum component within a reflection plane. If  $K$  is small, one alternating-parity sequence is favored. This is the case for the yrast sequences in even-even nuclei and the odd-mass nuclei with  $K = 1/2$  bands [6]. In the light actinide nuclei, parity-doublet sequences are reported for  $^{219}\text{Th}$  [6],  $^{223}\text{Th}$  [12],  $^{225}\text{Th}$  [13], and for some of the corresponding Ra isotones such as  $^{221}\text{Ra}$  [14], and these band structures are all consistent with a  $K \geq 3/2$  assignment. Parity-doublet sequences are notably absent in  $^{221}\text{Th}$  [12] and  $^{219}\text{Ra}$  [15]. These nuclei have yrast sequences that are assigned  $K = 1/2$  [16]. On the other hand, for alternating-parity sequences of non-yrast states with  $K \geq 3/2$ , the presence of parity doublets can be logically anticipated. This scenario has not yet been confirmed by experiment and is the subject of the present paper.

A detailed study of  $^{221}\text{Th}$  is of interest for the following reasons: (i) Due to the reported absence of parity doublets in the nucleus,  $^{221}\text{Th}$  is an exceptional case among the lighter Th isotopes. Judging from the level scheme of its isotone  $^{219}\text{Ra}$ , the non-yrast structure should contain two excited octupole sequences. Hence, delineation of the non-yrast structure of  $^{221}\text{Th}$  is desirable. (ii) The rapid decrease of the quadrupole-octupole collectivity around  $N = 130$  should lead to pronounced differences between the bands based on various quasiparticle states. (iii) The good simplex of the yrast sequence of  $^{221}\text{Th}$  leads to a concentration of decay intensity into a single band, similar to the observations in even-even nuclei. An issue that has not yet been discussed concerns the high-spin feeding of octupole sequences. For  $^{222}\text{Th}$ , an octupole to reflection-symmetric shape transition has been predicted at high spin [17], but the experimental study of this nucleus [18] has remained inconclusive. Hence, a corresponding study of  $^{221}\text{Th}$  is complementary.

Studies of  $^{221}\text{Th}$  and other light Th nuclei with spectroscopic methods have traditionally been performed with an additional “filter” device, in order to separate the  $\gamma$  rays emitted by the evaporation-residue (ER) nuclei from those of the dominant fission products and from other sources of background [12]. This approach has been chosen in the present study as well. The detector setup consisted of the Gammasphere spectrometer [19], comprising 98 high-purity germanium (HPGe) detectors with bismuth germanate (BGO) Compton suppression shields, and the 64-element ER detector HERCULES [20]. The nucleus of interest was populated via the four-neutron evaporation channel of the compound nucleus  $^{225}\text{Th}$ , and the present article reports on the complete  $^{221}\text{Th}$  level scheme. The yrast octupole sequence has been modified, as compared to Ref. [12], and has been extended up to spin-parity  $39/2^+$  and  $37/2^-$ . Here, the alternating-parity structure appears to be cut off, but an additional transition is present. The non-yrast level structures have been delineated as well. In particular, two alternating-parity sequences, elevated by about 400 keV relative to the yrast band, are observed. Early accounts of various results from the present study were presented in Refs. [8] and [21]. It should be noted that, very recently, a study of  $^{221}\text{Th}$  with a somewhat different approach than the one used here was reported [22]. It described results

consistent with those presented below for certain parts of the level scheme, but the present study expands the knowledge of this nucleus further.

## II. EXPERIMENTAL DETAILS AND ANALYSIS PROCEDURES

The experiment was performed at the ATLAS facility at Argonne National Laboratory, using the Gammasphere plus HERCULES detector combination. The  $^{221}\text{Th}$  nucleus was populated via the  $4n$  channel in the 96-MeV  $^{18}\text{O} + ^{207}\text{Pb}$  reaction. The target foil, isotopically enriched to 92.8% in  $^{207}\text{Pb}$ , had a surface density of  $470 \mu\text{g}/\text{cm}^2$ , and was supported by a carbon layer of  $7 \mu\text{g}/\text{cm}^2$  facing the incoming beam.

Gammasphere comprised 98 HPGe detectors with BGO Compton-suppression shields. These were arranged in 15 rings of constant angle  $\theta$  around the target, where  $\theta$  is the polar angle of a detector with respect to the incident beam direction. Six of the HPGe detectors did not have the Hevimet collimators installed because of geometrical constraints. The front of each HPGe detector was covered by a 0.25-mm Cu absorber to reduce unwanted target x rays. Compared to the “prototype” experiment of Ref. [7], a modified version of HERCULES was used (cf. Ref. [8]). The front of the HERCULES detector array was located 23.2 cm from the target and the device subtended polar angles ranging from  $6.6^\circ$  to  $26.8^\circ$  with respect to the beam axis. Of the 64 HERCULES elements, 63 were in place. The ER time of flight ranged from 91 to 126 ns, as determined by ER production from the front to the back of the target. Such a long time of flight required sweeping of the beam, which has a nominal period of 82.5 ns, in order to avoid overlap between signals from events generated in consecutive bursts. A period of 247.5 ns was chosen, which in turn allowed use of a hardware veto for unwanted scattered beam and fission events. Two parameters were measured with HERCULES: the aforementioned time of flight (of the reaction products and some remnant scattered beam), and the pulse-height signal from each detector hit by a particle. The event trigger required a prompt coincidence between a hit in a HERCULES detector and a minimum of two Compton-suppressed  $\gamma$ -ray events in Gammasphere.

The  $\gamma$  rays from ER nuclei were selected by two-dimensional gating on the HERCULES parameters. The energies of the  $\gamma$  rays were corrected for the Doppler shift by using the observed residue direction. The  $\gamma$ -ray energies of coincident transitions were then sorted into two- and three-dimensional histograms as specified further below.

The earlier study of the neighboring  $^{220}\text{Th}$  nucleus [7] showed that the  $4n$  channel leading to this nucleus had the largest ER yield. In the present experiment, however, the nucleus that is nominally associated with the  $\alpha 3n$  channel,  $^{218}\text{Ra}$ , is found to be most strongly populated, exceeding the yield of the channel of interest,  $^{221}\text{Th} + 4n$ , by a factor of 2. Note that incomplete fusion, from the  $^{207}\text{Pb}(^{14}\text{C}, 3n)$  reaction [23], is a contributor as well. The  $\alpha 2n$  channel leading to  $^{219}\text{Ra}$  also has considerable yield, but is a weaker competitor with respect to the  $4n$  channel, as are the  $^{220}\text{Th} + 5n$  and  $^{222}\text{Th} + 3n$  reactions. The following measures were taken to



TABLE I. Information on the  $\gamma$ -ray transitions in  $^{221}\text{Th}$ .

$I_i^\pi$ <sup>a</sup>	$E$ (keV) <sup>b</sup>	$E_\gamma$ (keV)	$I_\gamma$ <sup>c</sup>	$A_2/A_0$	$A_4/A_0$
<i>Ground-state sequence</i>					
11/2 <sup>+</sup>	251	250.9(1)	75.0(30)	0.152(29)	-0.035(34)
15/2 <sup>+</sup>	573	321.9(1)	34.9(12)	0.201(20)	-0.007(26)
15/2 <sup>+</sup>	573	84.9(2)	11.9(9)	-0.159(18)	0.029(21)
19/2 <sup>+</sup>	947	373.6(2)	8.3(3)	0.149(41)	-0.067(54)
19/2 <sup>+</sup>	947	199.8(2)	24.6(10)	-0.174(20)	0.020(26)
23/2 <sup>+</sup>	1356	409.5(3)	1.8(2)	0.237(21)	-0.041(30)
23/2 <sup>+</sup>	1356	277.4(2)	15.1(6)	-0.178(16)	0.022(23)
27/2 <sup>+</sup>	1777	420.6(3)	1.3(2)	0.284(43) <sup>d</sup>	
27/2 <sup>+</sup>	1777	304.4(2)	11.4(5)	-0.251(32)	0.033(38)
31/2 <sup>+</sup>	2211	433.7(3)	1.3(1)	0.36(13) <sup>d</sup>	
31/2 <sup>+</sup>	2211	274.8(2)	9.3(4)	-0.200(46)	-0.025(60)
35/2 <sup>+</sup>	2685	473.4(4)	2.9(2)	0.268(40)	-0.033(49)
35/2 <sup>+</sup>	2685	238.9(3)	6.3(3)	-0.192(44)	0.012(56)
39/2 <sup>+</sup>	3198	513.1(4)	2.1(3)	0.292(38)	-0.062(64)
39/2 <sup>+</sup>	3198	225.4(4)	1.7(3)	-0.218(52)	0.052(69)
(43/2 <sup>+</sup> )	3729	531(1)	0.8(2)		
<i>Sequence "a"</i>					
13/2 <sup>-</sup>	488	237.1(2)	35.9(19)	-0.183(14)	0.014(17)
17/2 <sup>-</sup>	747	259.1(2)	2.6(2)		
17/2 <sup>-</sup>	747	173.9(1)	37.0(14)	-0.201(19)	0.016(23)
21/2 <sup>-</sup>	1079	331.5(2)	12.4(5)	0.207(27)	-0.030(32)
21/2 <sup>-</sup>	1079	132.1(2)	17.3(9)	-0.190(23)	0.028(30)
25/2 <sup>-</sup>	1472	393.3(2)	13.7(6)	0.266(29)	-0.028(37)
25/2 <sup>-</sup>	1472	116.0(2)	5.7(4)	-0.202(26)	0.036(37)
29/2 <sup>-</sup>	1936	463.3(2)	9.6(5)	0.290(11)	-0.041(13)
29/2 <sup>-</sup>	1936	159.2(2)	5.0(3)	0.200(31)	0.023(39)
33/2 <sup>-</sup>	2445	509.3(4)	4.3(3)	0.295(26)	-0.043(32)
33/2 <sup>-</sup>	2445	234.5(3)	6.5(4)	-0.195(26)	-0.003(36)
37/2 <sup>-</sup>	2972	526.5(4)	1.4(2)	0.34(10) <sup>d</sup>	
37/2 <sup>-</sup>	2972	287.3(4)	2.7(3)	-0.230(37)	0.037(49)
<i>Sequence "b1"</i>					
15/2 <sup>-</sup>	992	254.4(3)	2.4(3)	-0.186(30)	0.030(39)
15/2 <sup>-</sup>	992	503.3(3)	1.4(2)	-0.102(15) <sup>d</sup>	
19/2 <sup>-</sup>	1366	374.2(3)	1.3(3)	0.226(35) <sup>d</sup>	
19/2 <sup>-</sup>	1366	221.5(2)	3.6(3)	-0.178(31)	0.043(58)
19/2 <sup>-</sup>	1366	618.3(4) <sup>e</sup>	3.3(4)	-0.103(20)	0.076(26)
23/2 <sup>-</sup>	1794	427.4(3)	2.3(4)		
23/2 <sup>-</sup>	1794	184.3(2)	3.2(3)	-0.214(34)	0.023(44)
23/2 <sup>-</sup>	1794	713.5(4) <sup>f</sup>	2.4(3)	-0.142(36)	0.088(47)
27/2 <sup>(-)</sup>	2165	209.4(3)	1.3(2)	-0.55(30) <sup>d</sup>	
<i>Sequence "b2"</i>					
13/2 <sup>+</sup>	737	485.9(2) <sup>g</sup>	6.4(5)	-0.145(41)	0.085(50)
17/2 <sup>+</sup>	1144	406.5(3)	1.4(2)	0.123(30)	-0.035(40)
17/2 <sup>+</sup>	1144	152.3(2)	1.6(2)	-0.188(27)	0.023(37)
17/2 <sup>+</sup>	1144	570.7(3)	1.5(3)	-0.29(20) <sup>d</sup>	
21/2 <sup>+</sup>	1608	464.4(3)	1.4(3)		
21/2 <sup>+</sup>	1608	242.6(2)	3.2(3)	-0.207(28)	0.032(37)
25/2 <sup>+</sup>	1954	345.6(4)	0.8(1)		
25/2 <sup>+</sup>	1954	161.9(3)	3.4(4)	-0.235(31)	0.039(39)
25/2 <sup>+</sup>	1954	599(1)	0.7(2)		
25/2 <sup>(+)</sup>	1985	191.8(3)	1.4(2)	-0.219(32)	-0.005(43)
<i>Sequence "c1"</i>					
	1098	609(1)	0.8(3)		
21/2 <sup>-</sup>	1442	695.3(3)	1.9(2)	0.394(83)	-0.114(104)
25/2 <sup>-</sup>	1814	371.4(4)	0.9(2)		

TABLE I. (*Continued.*)

$I_i^\pi$ <sup>a</sup>	$E$ (keV) <sup>b</sup>	$E_\gamma$ (keV)	$I_\gamma$ <sup>c</sup>	$A_2/A_0$	$A_4/A_0$
25/2 <sup>-</sup>	1814	125.3(2)	1.0(2)	-0.277(55)	0.041(88)
25/2 <sup>-</sup>	1814	735.0(3)	2.7(3)	0.315(34)	-0.089(47)
<i>Sequence "c2"</i>					
23/2 <sup>+</sup>	1689	246.4(3)	1.2(2)	-0.294(88)	-0.028(106)
23/2 <sup>+</sup>	1689	742.6(5)	1.0(3)	0.368(79)	-0.064(93)
27/2 <sup>(+)</sup>	2065	251(1)	$\geq 1.5$ <sup>h</sup>	-0.30(10) <sup>i</sup>	0.10(11) <sup>i</sup>
<i>Level group "d"</i>					
19/2	1625	879(1)	0.9(2)	-0.28(11) <sup>d</sup>	
(23/2)	1920	841(1)	0.8(2)		
(27/2)	2392	919(1)	0.5(2)		
<i>Level group "e"</i>					
(21/2)	1541	595.4(3)	0.7(2)		
21/2	1845	899(1)	0.8(2)	-0.34(11) <sup>d</sup>	
(25/2)	2205	849(1)	0.7(2)		
<i>Unplaced transition</i>					
		141.9(2)	1.1(2)		

<sup>a</sup>Spin and parity of the depopulated state.<sup>b</sup>Energy of the depopulated state.<sup>c</sup>Relative  $\gamma$ -ray intensity of the transition normalized to 75 for the 250.9-keV transition.<sup>d</sup>No  $A_4$  coefficient extracted.<sup>e</sup> $E2/M1$  mixing ratio  $\delta = 0.10(+4 - 8)$ .<sup>f</sup> $\delta = 0.10(+3 - 6)$ .<sup>g</sup> $\delta = 0.10(+4 - 6)$ .<sup>h</sup>Lower limit due to the presence of an unresolved doublet.<sup>i</sup>Approximate value (obtained by gating on 250.9-keV line).

rays seen in the previous spectrum. The latter transition has been misplaced in the level scheme of Ref. [12]: it cannot be placed in the yrast sequence. The spectrum gated by the 486-keV transition [Fig. 2(c)] indicates that this  $\gamma$  ray is in coincidence with only one of the yrast transitions: the 251-keV line. In the same spectrum, some weaker  $^{221}\text{Th}$  transitions with respective energies of 152, 162, 184, 222, 243, 254, and 407 keV are found to be enhanced; these give rise to the structures labeled as "b1" and "b2" in Fig. 1. Unfortunately, the spectrum of Fig. 2(c) suffers from contaminations by the  $^{218}\text{Ra} + \alpha 3n$  channel [29] and a target impurity leading to  $^{219}\text{Ac}$  [30]. However, the present set of weaker transitions in  $^{221}\text{Th}$  is not established by the 486-keV  $\gamma$  ray alone, as discussed further below.

The spectra of Fig. 3 are relevant for the modification of the yrast sequence at medium spin with respect to Ref. [12], and for its extension towards the highest spins observed. Here, the gating transitions are chosen to be those of  $E1$  character, which compete favorably for strength with the bypassing  $E2$   $\gamma$  rays. The 275-keV ( $31/2^+ \rightarrow 29/2^-$ ) and 239-keV ( $35/2^+ \rightarrow 33/2^-$ ) transitions are placed in the level scheme in agreement with Ref. [22]. Their respective coincidence spectra demonstrate the absence/presence of specific  $E2$  transitions. For example, in Fig. 3(a), the 509-keV transition is absent, but present in Fig. 3(b). Equally important, the spectra of Figs. 3(a) and 3(b) indicate the gradual growth of important high-spin transitions; e.g., the 287-keV line, missed previously.

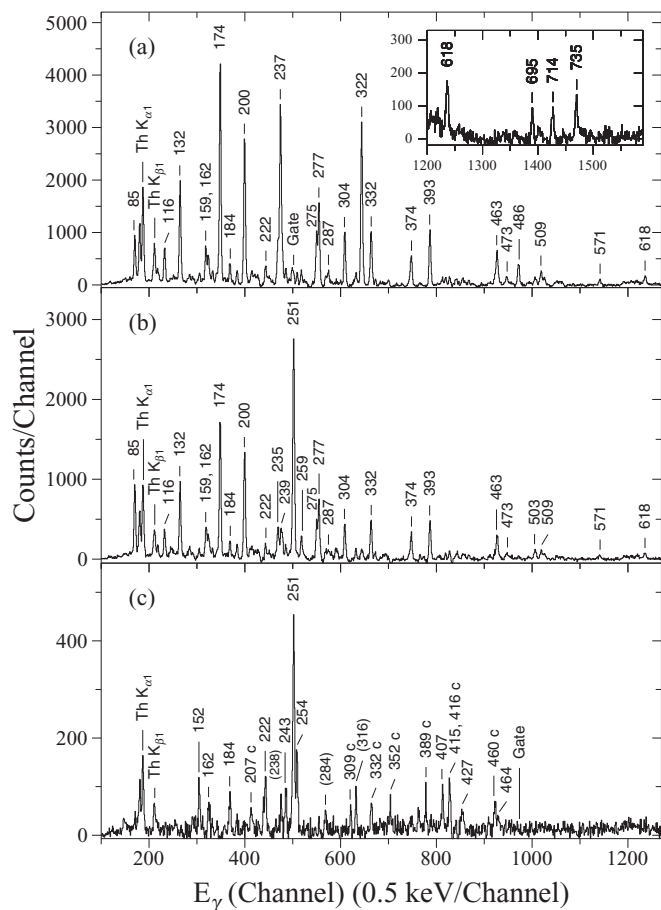


FIG. 2. Representative ER-gated  $\gamma$ -ray coincidence spectra for  $^{221}\text{Th}$ . The gating  $\gamma$ -ray transitions have the respective energies of (a) 251, (b) 237, and (c) 486 keV. The inset in panel (a) displays a fraction of the spectrum highlighting coincident transitions above 600 keV. The spectrum in panel (c) is contaminated by  $\gamma$  rays from  $^{218}\text{Ra}$ , labeled by “c”, and from  $^{219}\text{Ac}$ , given in parentheses.

A spectrum gated by the latter transition is displayed in Fig. 3(c). The most significant features of this spectrum are: the growth of the 225-keV line, as compared to Fig. 3(b), the presence of the 531-keV  $\gamma$  ray, and the absence of the 513-keV transition. The latter is hereby validated as an  $E2$  crossover transition.

In Fig. 9, the angular distributions are presented for some of the transitions that lead to the extension of the yrast sequence from medium to high spin. Specifically, the data for the 235- (33/2<sup>-</sup> → 31/2<sup>+</sup>), 509- (33/2<sup>-</sup> → 29/2<sup>-</sup>), and 287-keV (37/2<sup>-</sup> → 35/2<sup>+</sup>) transitions are shown; they document the corresponding entries in Table I and support the discussion in the previous paragraph.

The spectra of Fig. 4 support the placement of the highest-lying transitions in  $^{221}\text{Th}$ . In panel (a), all transitions placed below the 225-keV gating  $\gamma$  ray are present with comparable strength, while the 513-keV line is absent. In addition, growth of the 531-keV line is observed when the spectrum is compared with that of Fig. 3(c). The coincidence relationships between the 531-keV line and transitions in  $^{221}\text{Th}$  are further investigated in Figs. 4(b) and 4(c). These

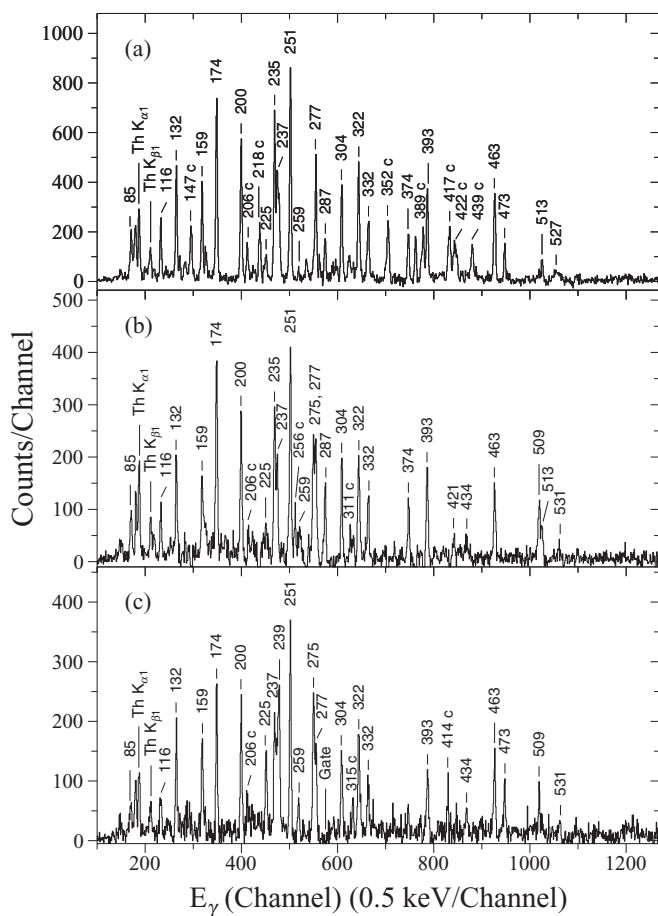


FIG. 3. Similar to Fig. 2, but for gating transitions with the respective energies of (a) 275, (b) 239, and (c) 287 keV. Contaminant  $\gamma$  rays are labeled by “c” and are from  $^{218}\text{Ra}$  in spectra (a) and (c), but from  $^{222}\text{Th}$  in spectrum (b).

spectra suffer from the proximity of the gating  $\gamma$  ray to a transition in  $^{219}\text{Ra}$ . However, as illustrated in panel (b), the  $^{219}\text{Ra}$  contributions to the spectrum can be subtracted, and the net spectrum contains the prominent transitions of the yrast sequence and, due to a second contaminant, some lines in  $^{220}\text{Th}$  [7]. The coincidence spectrum before subtraction is shown in panel (c) for completeness. The 531-keV line is the top-most transition in  $^{221}\text{Th}$  observed in the present work. However, the transition breaks the trend of the yrast sequence in that a relatively strong ( $E_\gamma \lesssim 300$  keV)  $E1$   $\gamma$  ray is absent above the 39/2<sup>+</sup> state. A reasonable spin-parity assignment for the 3729-keV level established by this 531-keV  $\gamma$  ray is either 41/2<sup>+</sup> or 43/2<sup>+</sup>. Unfortunately, angular-distribution information is not available because of the small intensity. For all the lower-lying transitions, such information is provided in Table I.

*Structures “b1” and “b2”* : The placement of transitions in structures “b1” and “b2” depends crucially on their coincidence relationships with some high-energy ( $E_\gamma \gtrsim 600$  keV) dipole transitions. These linking transitions are highlighted in the inset of Fig. 2(a), and the coincidence spectra for the 618- and 714-keV  $\gamma$  rays are displayed in Figs. 5(a) and 5(c),

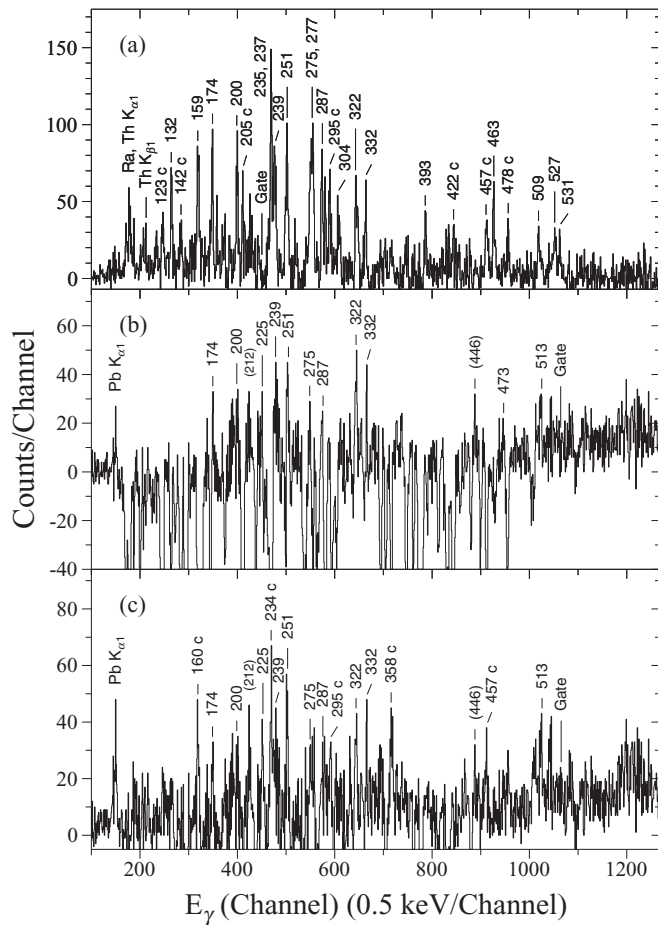


FIG. 4. Similar to Fig. 2, but for gating transitions with the respective energies of (a) 225, and both (b) and (c) 531 keV (see text). Contaminant  $\gamma$  rays labeled by “c” are from  $^{219}\text{Ra}$ .

respectively. The spectrum of Fig. 5(a) determines the placement of the 243-keV ( $21/2^+ \rightarrow 19/2^-$ ) transition, and suggests that the 184- and 162-keV lines are next in the sequence. The spectrum also provides evidence for the 427-keV  $\gamma$  ray that bypasses two of the former transitions. The spectrum of Fig. 5(b) confirms the coincidence relationship between the 243- and 618-keV transitions. In addition, it provides evidence for the 374-keV bypassing transition that is placed below the gating  $\gamma$  ray, even though a part of the spectrum is contaminated by peaks from  $^{218}\text{Ra}$ . The coincidence spectrum of Fig. 5(c) leads to the placement of the 162-keV transition above spin 23/2. The spectrum also provides evidence for additional, weak transitions in this spin range with the respective energies of 192 and 209 keV. This can also be seen in the spectrum of Fig. 5(b).

The remaining ambiguities in the placement of transitions at the bottom and top of structures “b1” and “b2” have been clarified with the help of the ER-gated “cube” data, and spectra resulting from  $\gamma$ -ray double gates are displayed in Fig. 6. The spectrum in panel (a) supports the placement of the 254-keV transition at the bottom of the structure, and provides evidence for the presence of the bypassing 464-keV  $\gamma$  ray. Panel (b) provides additional evidence for the top part of the structure,

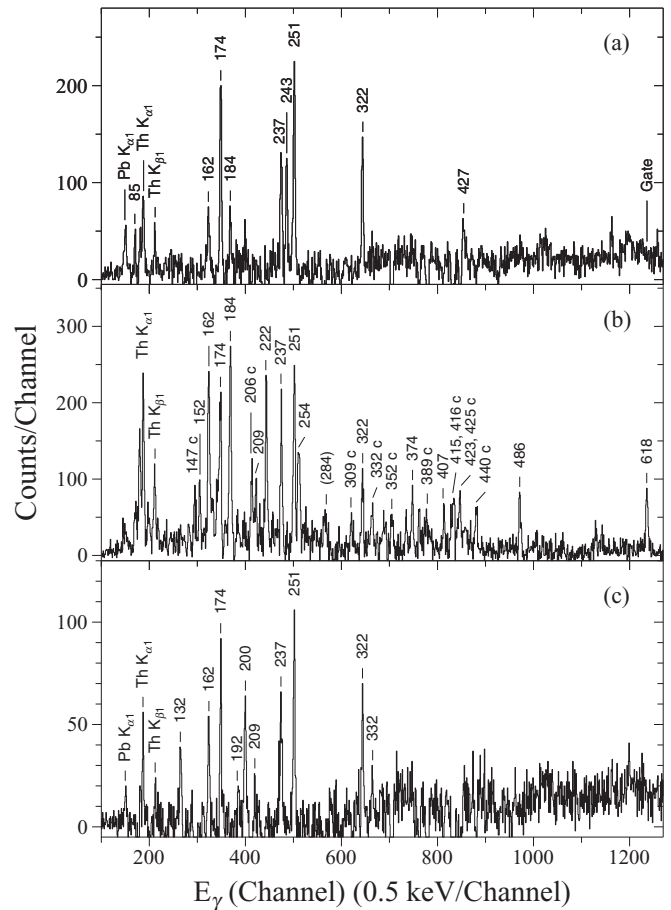


FIG. 5. Similar to Fig. 2, but for gating transitions with the respective energies of (a) 618, (b) 243, and (c) 714 keV. The spectrum in panel (b) is contaminated by  $\gamma$  rays from  $^{218}\text{Ra}$ , labeled by “c”.

including the 346-keV bypassing transition. The placement of the 209-keV  $\gamma$  ray above spin 25/2 is based on a triple-coincidence relationship between this line and the 162- and 714-keV  $\gamma$  rays (not shown). Such a relationship is absent for the 192-keV  $\gamma$  ray, seen in Fig. 5(c), which is placed in parallel with the 162-keV transition.

In Fig. 10, the angular distributions for some of the  $\gamma$  rays that are crucial for the construction of structure “b1” and “b2” are presented. Specifically, the angular distributions for the 486- ( $13/2^+ \rightarrow 11/2^+$ ), 152- ( $17/2^+ \rightarrow 15/2^-$ ), and 618-keV ( $19/2^- \rightarrow 17/2^-$ ) lines are given. The 486- and 618-keV linking transitions have large positive  $A_4/A_0$  coefficients compared to the 152-keV line of  $E1$  character. The former two  $\gamma$  rays are viewed as typical examples of  $M1$  transitions in the present level scheme. For these and the 714-keV ( $23/2^- \rightarrow 21/2^-$ ) transition,  $E2/M1$  mixing ratios,  $\delta$ , have been extracted; their values are included in Table I as footnotes.

The negative-parity assignment for sequence “b1” is also supported by the absence of a competing  $E2$  transition from, e.g., the level from which the 254-keV line originates to a final state located in another sequence. If the former level was of positive parity, a fairly strong transition to the  $11/2^+$  state with  $E_\gamma = 740$  keV would be expected, but such a line is absent [see inset of Fig. 2(a)].

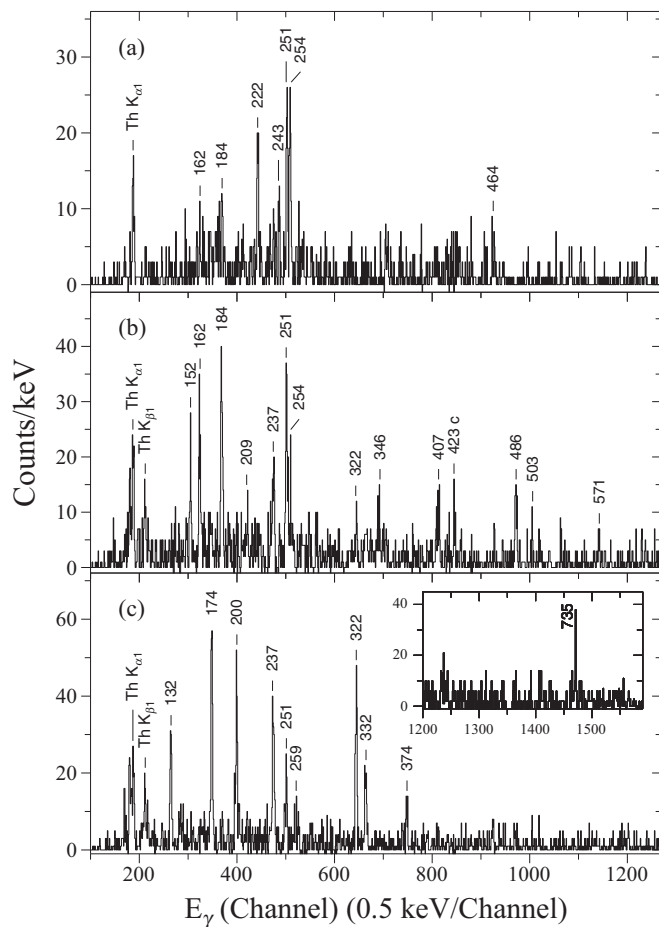


FIG. 6. Sample ER-gated and  $E_\gamma$ - $E_\gamma$  double-gated spectra. The combinations of the gating transitions are (a) 152–486 keV, (b) 222–243 keV, and (c) 251–735 keV and 251–251 keV for the spectra in the main panel and the inset, respectively. The 423-keV line in spectrum (b) is a  $^{218}\text{Ra}$  contaminant.

*Structures “c1” and “c2”* : These two structures are established through the presence of high-energy  $E2$  transitions with respective energies of 695, 735, and 743 keV. The coincidence spectrum for the first transition is displayed in Fig. 7(a): it determines the placement of the 246-keV ( $23/2^- \rightarrow 21/2$ )  $\gamma$  ray and suggests the presence of a 371-keV line. The spectrum of Fig. 7(b) confirms the coincidence relationship between the 246- and 695-keV  $\gamma$  rays, where the latter is shown in the inset. In addition, the spectrum displays a new, 125-keV transition and, at the same time, indicates the absence of a 371-keV line. This suggests the placement of the 246- and 125-keV transitions on top of each other, bypassed by a 371-keV  $\gamma$  ray. Additional support for these levels comes from the coincidence spectra for the 735- and 743-keV transitions, with the former seen in Fig. 7(c). This spectrum is also indicative of an enhanced 251-keV line, when compared to the spectrum of Fig. 7(a). As mentioned earlier, the 251-keV ground-state transition is self-coincident [cf. Fig. 2(a)], and the placement of the second 251-keV  $\gamma$  ray on top of the 735-keV line is proposed. This hypothesis is validated by the doubly-gated spectra presented in Fig. 6(c).

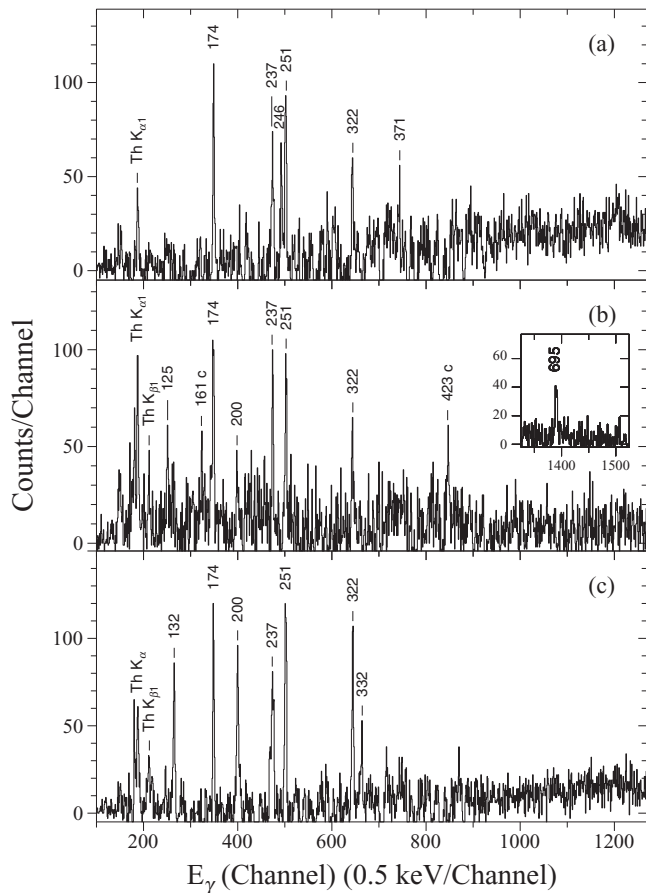


FIG. 7. Similar to Fig. 2, but for gating transitions with the respective energies of (a) 695, (b) 246, and (c) 735 keV. The contaminants in spectrum (b), labeled by “c”, are attributed in part to  $^{218}\text{Ra}$ . The inset in this panel highlights the coincident 695-keV transition.

Here, the main part of the panel presents the spectrum for the 251–735 keV combination of gating transitions, which brings back the 251-keV  $\gamma$  ray. In the inset of the panel, a part of the spectrum for the 251–251 keV combination is provided, in order to demonstrate that, among the relevant high-energy transitions [cf. Fig. 2(a)], only the 735-keV line survives the gating procedure.

In Fig. 11, the angular distributions for some of the transitions that are crucial for the construction of structures “c1” and “c2” are presented. Specifically, distributions are given for the 246- ( $23/2_2^+ \rightarrow 21/2_2^-$ ), 735- ( $25/2_2^- \rightarrow 21/2_1^-$ ), and 743-keV ( $23/2_2^+ \rightarrow 19/2^+$ )  $\gamma$  rays.

Even though structures “c1” and “c2” are shorter than the “b1” and “b2” ones, the pattern of  $E1$  and crossover  $E2$  transitions is suggestive of an octupole sequence; i.e., it exhibits the characteristic “zigzag” pattern. The similarity between both structures includes the pattern of linking transitions to the yrast sequence, though the multiplicities differ. A tentatively placed 609-keV  $\gamma$  ray at somewhat lower spin may be viewed as part of these “c1” and “c2” structures. The initial state is not connected, however, and a transition from “c1” to this state may well be too weak to be observed in the present work.

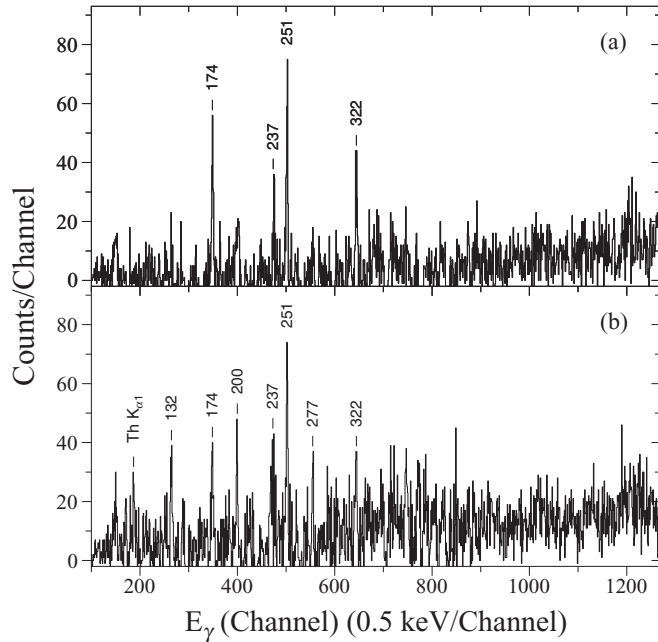


FIG. 8. Similar to Fig. 2, but for gating transitions with the respective energies of (a) 879 and (b) 849 keV.

In Fig. 12, the decay intensities of the states belonging to the octupole band structures are plotted as functions of spin after correction for internal conversion using the tabulation of Ref. [31]. Not only are the structures “b1”, “b2” and “c1”, “c2” of lower intensity than the yrast band by factors of 5 to 8, but they also exhibit different intensity profiles due to the decay-out through linking transitions. Structures “c1”, “c2” lose most of their intensity through the 735-keV ( $25/2_2^- \rightarrow 21/2_1^-$ )  $\gamma$  ray and, thus, carry less intensity below spin 25/2 than the structures “b1”, “b2”. The intensity plots for the yrast band and structures “b1”, “b2” indicate, for parts of the sequences, a spin-dependent staggering. This, however, does not compromise the feeding and decay intensity of a particular level: the latter is always larger than or equal to the former.

*Other non-yrast levels:* The level scheme contains additional non-yrast levels that have been grouped into two sets labeled “d” and “e”. These do not form independent sequences; i.e., they are not connected to each other, nor are they linked to one of the non-yrast sequences “b1”, “b2” or “c1”, “c2”. The difference between sets “d” and “e” is that one decays by high-energy transitions to the negative-parity states of the yrast sequence, while the other feeds positive-parity levels. An example for the former decay mode is the 879-keV transition, for which a coincidence spectrum can be found in Fig. 8(a). An example for the decay to a positive-parity yrast state is the 849-keV  $\gamma$  ray, with the corresponding spectrum introduced in Fig. 8(b). For the 879- and 899-keV transitions, angular distributions could be measured, indicating a dipole character for both. The other transitions in this part of the level scheme are tentatively assigned a dipole character by analogy with the former two, backed also by intensity considerations. For example, an  $E2$  assignment for the 595-keV line is deemed

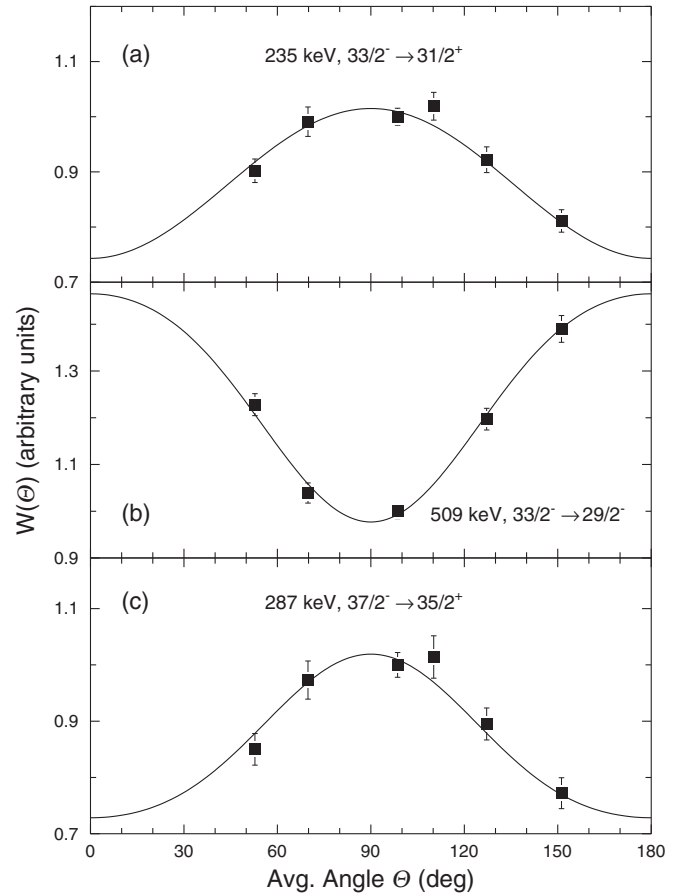


FIG. 9. Representative  $\gamma$ -ray angular distributions for yrast transitions in  $^{221}\text{Th}$ . Panels (a)–(c) are for the 235-, 509-, and 287-keV transitions, respectively. Some of the error bars are within the size of the symbols. The  $A_k$  ( $k = 2, 4$ ) coefficients, obtained from Legendre-polynomial fits and normalized to  $A_0$ , are given in Table I.

unlikely; otherwise the emitting level would be more strongly populated than the  $23/2_2^+$  state of structures “c1”, “c2”.

*Additional level information:* A tentatively reported level at 47 keV [26] could not be confirmed from the present data nor was any indication found for a transition that would bypass the 251-keV ( $11/2^+ \rightarrow 7/2^+$ )  $\gamma$  ray. A weak 142-keV line could not be placed in the level scheme due to its closeness to a  $^{219}\text{Ra}$  contaminant.

*$B(E1)/B(E2)$  ratios:* Figure 13 introduces the  $B(E1)/B(E2)$  probability ratios, determined from the  $\gamma$ -ray intensities, and displays these as a function of the initial spin for the yrast (a) and non-yrast (b) transitions in  $^{221}\text{Th}$ . The ratios obtained for the two major parts of the level scheme are on average very similar:  $\overline{B(E1)/B(E2)} = 2.17(24) \times 10^{-6} \text{ fm}^{-2}$  and  $2.28(37) \times 10^{-6} \text{ fm}^{-2}$  for the yrast band and structures “b1”, “b2” and “c1”, “c2”, respectively. The error ranges associated with the average values are indicated in Fig. 13 as well. These results are also reported in Table II.

The  $B(E1)/B(E2)$  ratios for the yrast transitions exhibit at medium spin ( $21/2 \leq I \leq 31/2$ ) a distinct pattern, where values for initial states with positive parity lie systematically above those for negative-parity levels. This observation implies

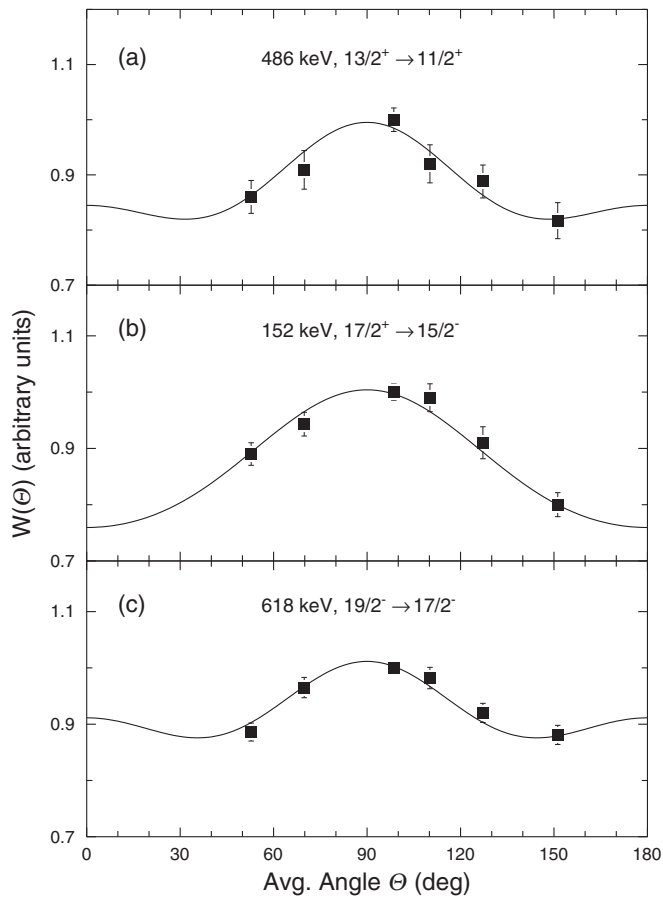


FIG. 10. Similar to Fig. 9, but for transitions in the sequences “b1” and “b2” (see text). The transitions have the respective energies of (a) 486, (b) 152, and (c) 618 keV.

that the population of a subsequent negative-parity state is enhanced and, thus, this pattern is consistent with the staggering effect mentioned above for a part of Fig. 12. The data presented in Fig. 13(b) have comparatively large errors and no indication of a parity-dependent staggering is found.

*B(M1)/B(E2) ratios:* For transitions from the  $19/2^-$  and  $23/2^-$  states,  $B(M1)/B(E2)$  probability ratios have been determined, where the corresponding mixing ratios  $\delta$  given in footnotes e and f of Table I were used. These ratios are presented in Fig. 14, and compared with related information for  $^{223}\text{Th}$  and  $^{219}\text{Ra}$ . For  $^{221}\text{Th}$ , the average value is  $\overline{B(M1)/B(E2)} = 3.44(65) \times 10^{-6} \mu_N^2/(e^2\text{fm}^4)$ , where  $\mu_N$  is the nuclear magneton; the value and the corresponding error are indicated in the figure.

#### IV. DISCUSSION

In this section, the alternating-parity sequences in  $^{221}\text{Th}$  are labeled in terms of the simplex quantum number and, guided by the theoretical studies of Refs. [32,33], neutron configurations are proposed. Comparisons with neighboring isotones and odd- and even-mass isotopes are discussed, where the following quantities are presented in a systematic way: relative energies between band structures, spin alignments,

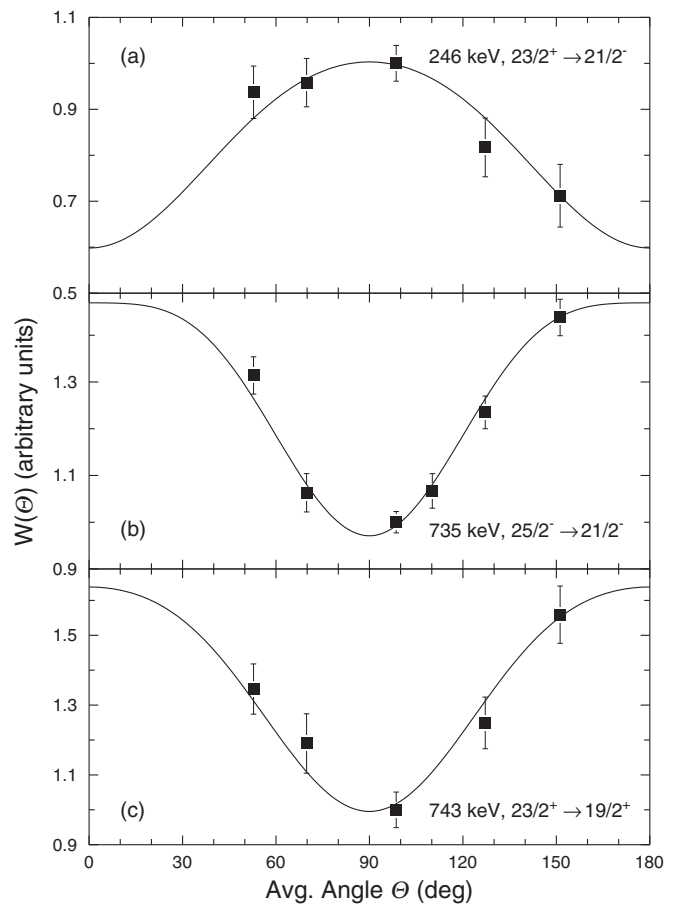


FIG. 11. Similar to Fig. 9, but for transitions in the sequences “c1” and “c2” (see text). The transitions have the respective energies of (a) 246, (b) 735, and (c) 743 keV.

$B(E1)/B(E2)$  and  $B(M1)/B(E2)$  ratios, and parity splittings. Note that there is conflicting information on the level scheme of  $^{219}\text{Ra}$ , as has been discussed in Refs. [15,34]. The difference lies in the spin assignment for the lowest yrast transition. In the present discussion, the data from Ref. [15] are used, for two reasons: (i) A key aspect of the discussion focusses on the  $B(E1)/B(E2)$  and  $B(M1)/B(E2)$  ratios, which, in the case of  $^{219}\text{Ra}$ , are based on Ref. [15]. (ii) Choosing Ref. [34] instead would complicate the comparison with neighboring nuclei.

The combination of the ground-state  $E2$  sequence and sequence “a” represents the simplex quantum number  $s = -i$ . The non-yrast structures “b1”, “b2” and “c1”, “c2” can be associated with  $s = +i$  and  $s = -i$ , respectively. The degree of parity doubling is measured by the excitation energies of these bands relative to each other as well as by their spin-alignment properties. The latter provide useful information about the value of the  $K$  quantum number.

Figure 15 displays on a relative scale the excitation energies of octupole bands in odd-mass Th nuclei, as well as in some of their Ra isotones, as a function of the spin. The ordinate values are consistently derived from the energy difference,  $E_{\text{rel}} = E(I, s = +i) - E(I, s = -i)$ , between each state in the  $s = +i$  and  $s = -i$  bands of the nucleus. Except for  $^{221}\text{Th}$  and  $^{219}\text{Ra}$ , the  $s = \pm i$  sequences are yrast bands, are close

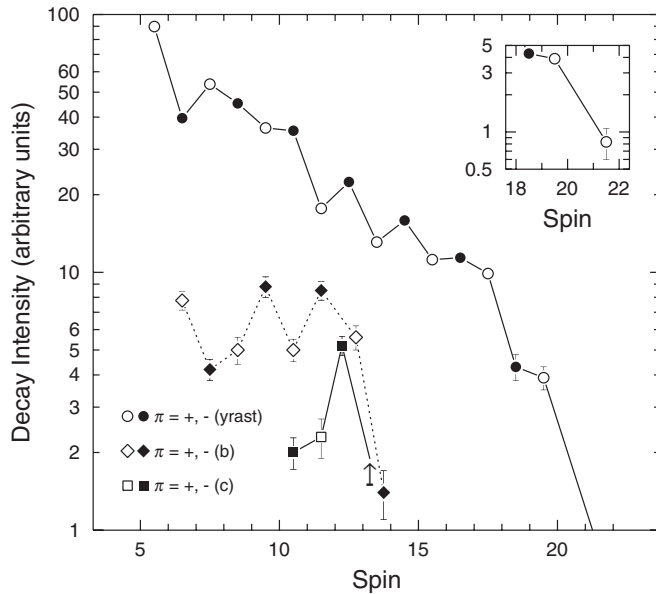


FIG. 12. Decay intensity versus spin for the states of the octupole-band structures in  $^{221}\text{Th}$ . The yrast band, and the structures “b1”, “b2”, and “c1”, “c2” are represented by circles, diamonds, and squares, respectively. The states are further distinguished by open and filled symbols for positive and negative parity, respectively. Some of the error bars are within the size of the symbols. The inset provides the intensity of the yrast band at the highest spins.

together, and form parity doublets. In the case of  $^{221}\text{Th}$ , the data points are derived from the set of  $s = \pm i$  non-yrast bands, as emphasized by a different choice of symbols in the figure. In addition, the function  $E_{\text{rel}}$  for the  $s = +i$  and the  $s = -i$  yrast sequence is given in the panel. In the  $^{219}\text{Ra}$  panel, again  $E_{\text{rel}}$  for the set of non-yrast and yrast bands is plotted (line, no symbol). The energy difference for the non-yrast bands in  $^{221}\text{Th}$  is comparatively close to 0 ( $E_{\text{rel}} \sim 100$  keV), and mirrors to a degree the parity doubling of the nearly degenerate  $s = \pm i$  bands in  $^{219}\text{Th}$ ,  $^{223}\text{Th}$ , and  $^{225}\text{Th}$  (dotted line). This finding is in contrast to the large energy differences between the  $s = +i$  sequence and the yrast band ( $E_{\text{rel}} \gtrsim 400$  keV). The simplex splittings suggest that the yrast sequence has  $K = 1/2$  and the excited bands “b1”, “b2” and “c1”, “c2” combine into a parity doublet with  $K > 1/2$ .

In the present context, it is important to recall that the  $s = +i$  sequence decays to the yrast band via high-energy  $M1$  transitions. The expected  $M1$  linking transitions from the  $s = +i$  band to the non-yrast  $s = -i$  band cannot compete with these high-energy  $\gamma$  rays as the two latter sequences lie close in energy. For example, a possible  $23/2^- \rightarrow 21/2_2^-$  transition ( $\Delta E = 352$  keV) is expected to be reduced in intensity to 10% of the rather weak  $23/2^- \rightarrow 21/2_1^-$   $\gamma$  ray ( $E_\gamma = 714$  keV); i.e., below the detection sensitivity of the measurement. Thus, a lack of linking transitions between nearly degenerate structures of different simplex value, a feature that has been observed before [6,12], is due to the  $s = \pm i$  doublets being non-yrast in this instance.

Figure 16 provides comparisons of the yrast octupole bands in the  $^{221}\text{Th}$ – $^{219}\text{Ra}$  and  $^{223}\text{Th}$ – $^{221}\text{Ra}$  isotonic pairs with similar

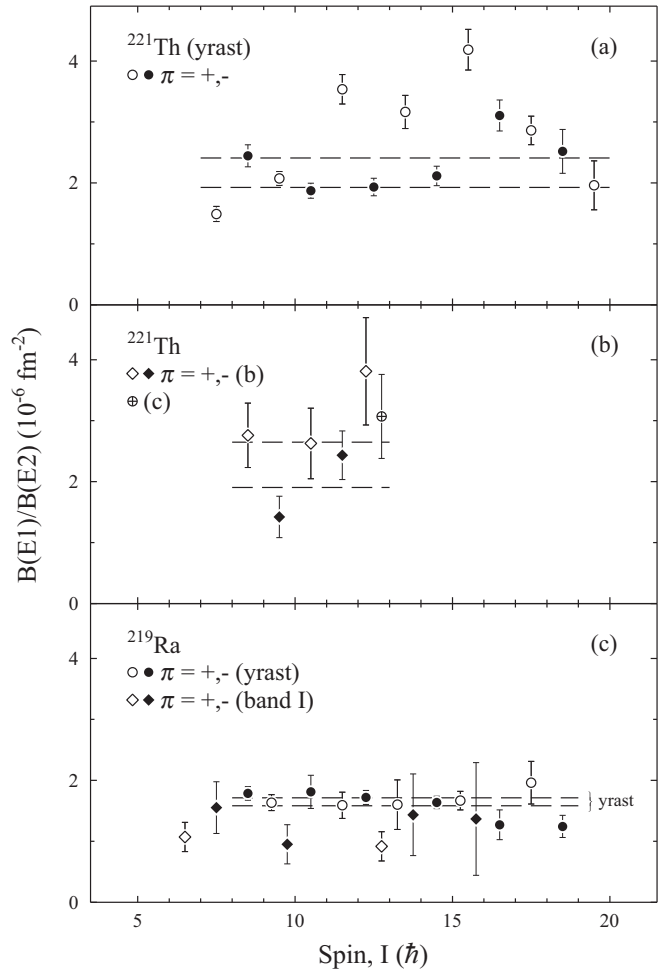


FIG. 13. (a)  $B(E1)/B(E2)$  ratios versus initial spin for yrast transitions in  $^{221}\text{Th}$ . The states are further distinguished by open and filled symbols for positive and negative parity, respectively. The horizontal bar represents the range of the error associated with the weighted average of all ratios. (b) Same, but for the non-yrast transitions. This data set represents essentially transitions in structure “b1”, “b2” (diamonds). (c) Combined plot for transitions in  $^{219}\text{Ra}$ , based on Ref. [15], for comparisons used in the discussion.

bands in the corresponding even-mass isotopes heavier by one mass unit, by plotting the initial spins vs the rotational frequency  $\omega$  ( $\hbar\omega = 1/2[E(I) - E(I - 2)]$ ). The purpose of these comparative plots is to demonstrate a distinct difference with respect to the corresponding behavior of the non-yrast bands in  $^{221}\text{Th}$  and  $^{219}\text{Ra}$  (see below). The data for the even-mass nuclei in Fig. 16 are from Refs. [18] ( $^{222}\text{Th}$ ,  $^{220}\text{Ra}$ ), [35] ( $^{224}\text{Th}$ ), and [36] ( $^{222}\text{Ra}$ ), and they are also shown in the spin vs frequency plot of Fig. 17. The negative-parity  $E2$  sequence of these nuclei is displayed as a reference with each odd-mass nucleus. This choice is guided by the fact that the negative-parity states in these nuclei are, at medium and high spin, lower in energy than the positive-parity levels. (See the parity splitting presented in Fig. 19.) The functions  $I(\omega)$  for the  $^{221,222}\text{Th}$  and  $^{219,220}\text{Ra}$  yrast bands all behave in a similar way: the frequency  $\omega$  gradually increases with the angular

TABLE II. Weighted-average values of  $B(E1)/B(E2)$  ratios obtained for  $^{221}\text{Th}$  and neighboring nuclei. For  $^{221}\text{Th}$  and  $^{219}\text{Ra}$ , two separate entries are provided for the yrast band and the non-yrast structures, respectively. The former entries are labeled y, for the latter a different label is used in accordance with Sec. III and with Ref. [15]. Such a distinction is not needed for the remaining nuclei.

Nucleus	Spin range or spins	$\overline{B(E1)/B(E2)}$ ( $10^{-6}\text{fm}^{-2}$ )	Reference
$^{221}\text{Th}$ (y)	$15/2 \leq I \leq 39/2$	2.17 (24)	This work
$^{221}\text{Th}$ (b, c)	$17/2 \leq I \leq 25/2$	2.28 (37)	This work
$^{223}\text{Th}$	$I = 11/2, 15/2, 19/2, 21/2,$ $23/2, 27/2, 29/2^a$	1.68 (32)	[12]
$^{225}\text{Th}$	$17/2 \leq I \leq 27/2$	0.83 (31)	[13]
$^{219}\text{Th}$	$15/2 \leq I \leq 21/2$	1.26 (81) <sup>b</sup>	[6]
$^{219}\text{Ra}$ (y)	$17/2 \leq I \leq 37/2$	1.65 (7)	[15]
$^{219}\text{Ra}$ (I)	$I = 13/2, 15/2, 19/2, 25/2,$ $27/2, 31/2^a$	1.07 (28)	[15]
$^{221}\text{Ra}$	$17/2 \leq I \leq 27/2$	0.93 (14)	[14]

<sup>a</sup> $B(E1)/B(E2)$  values are not obtained for consecutive spins.

<sup>b</sup>Weighted average of the reported values for structures  $s = +i$  and  $s = -i$ .

momentum  $I$ , which is characteristic for the heavier pairs  $^{223,224}\text{Th}$  and  $^{221,222}\text{Ra}$ .

Figure 18 presents analogous comparisons for the non-yrast bands in  $^{221}\text{Th}$  and  $^{219}\text{Ra}$ . However, in contrast to the situation above, these bands mimic the vibrational-like behavior of the respective even-mass isotopes lighter by one mass unit. The data for the latter are from Refs. [7] ( $^{220}\text{Th}$ ) and [29] ( $^{218}\text{Ra}$ ). The plots of the  $^{221}\text{Th}$  non-yrast bands show also the onset of a backbending at  $I > 11$ , seen in  $^{220}\text{Th}$ , but not in  $^{218}\text{Ra}$ . This

close similarity between band structures in different nuclei is quite remarkable. It strongly suggests that, in this instance, the odd particle acts as a spectator. In addition, the closeness of the different  $^{221}\text{Th}$  data points in Fig. 18(a) is consistent with the parity-doublet behavior of the non-yrast sequences discussed earlier.

In the light-actinide region, quadrupole deformation increases with mass. The deformation changes most rapidly around  $N = 130$ . As illustrated in Fig. 17, for the  $N = 130$  isotones, the frequency  $\omega$  fluctuates around a constant value, which is characteristic of small quadrupole collectivity. For  $N = 132$ ,  $\omega$  increases in a regular way, which signals a larger quadrupole collectivity. In such a transitional region, the odd particle would be expected to be shape driving. Hence, the similarities between, on the one hand, the  $^{221}\text{Th}$  non-yrast and  $^{220}\text{Th}$  yrast bands and, on the other, the  $^{221}\text{Th}$  and  $^{222}\text{Th}$  yrast bands suggest that the non-yrast sequences are less deformed than their yrast counterparts. This then provides a natural explanation for the non-yrast nature of structures “b1”, “b2” and “c1”, “c2”. The following paragraphs will corroborate this interpretation further by an analysis of the quasiparticle composition.

The authors of Refs. [32,33] investigated the low-spin structure of reflection-asymmetric, odd-mass nuclei in the light-actinide region in the framework of the microscopic-macroscopic mean-field approach. Both sets of calculations focus on the band-head configurations of octupole bands and lead to the same interpretation for the lowest one-quasiparticle state (yrast) in each nucleus. Those of Ref. [33], however, provide more specifics for ground-state and excited configurations in a particular nucleus and, thus, are more useful for configuration assignments. The calculations assume an axial, static shape determined by minimizing the energy of each configuration with respect to the set of deformation parameters  $\beta_2, \beta_3, \dots, \beta_7$ . The calculated single-particle states in the Woods-Saxon potential are labeled by the angular momentum projection  $\Omega$  on the symmetry axis and a quantum number  $n_\Omega$  that counts single-particle orbitals in increasing order of energy. For  $N = 131$ , the following neutron states are near the Fermi level:  $\Omega = 3/2$ ,  $n_\Omega = 17$  and  $\Omega = 5/2$ ,

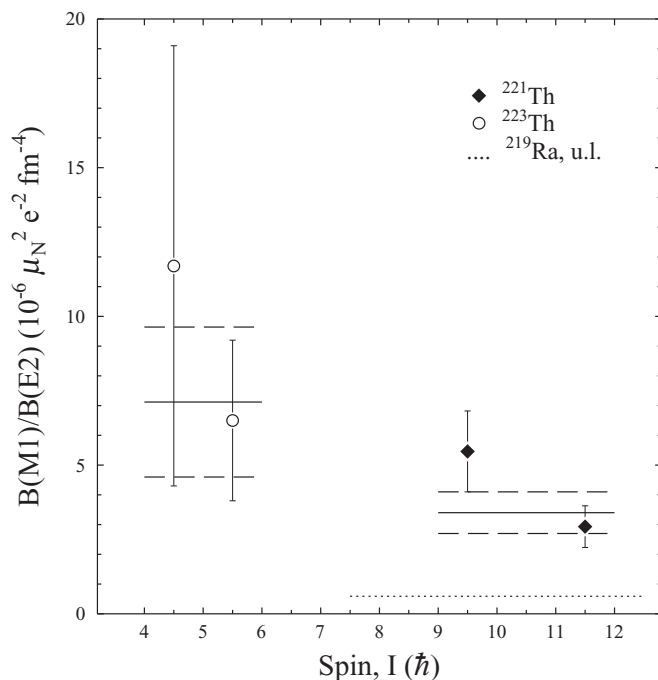


FIG. 14.  $B(M1)/B(E2)$  ratios versus initial spin for transitions from the  $19/2^-$  and  $23/2^-$  states in  $^{221}\text{Th}$  (diamonds) and for certain levels in  $^{223}\text{Th}$  (circles) [12] and  $^{219}\text{Ra}$  (single dotted line) [15]. The bands joining the groups of  $^{221}\text{Th}$  and  $^{223}\text{Th}$  data points represent the weighted averages of these ratios and their errors. For  $^{219}\text{Ra}$ , only an upper limit (abbreviated u.l.) is available. The spin range has been truncated at the upper end (cf. Table IV).

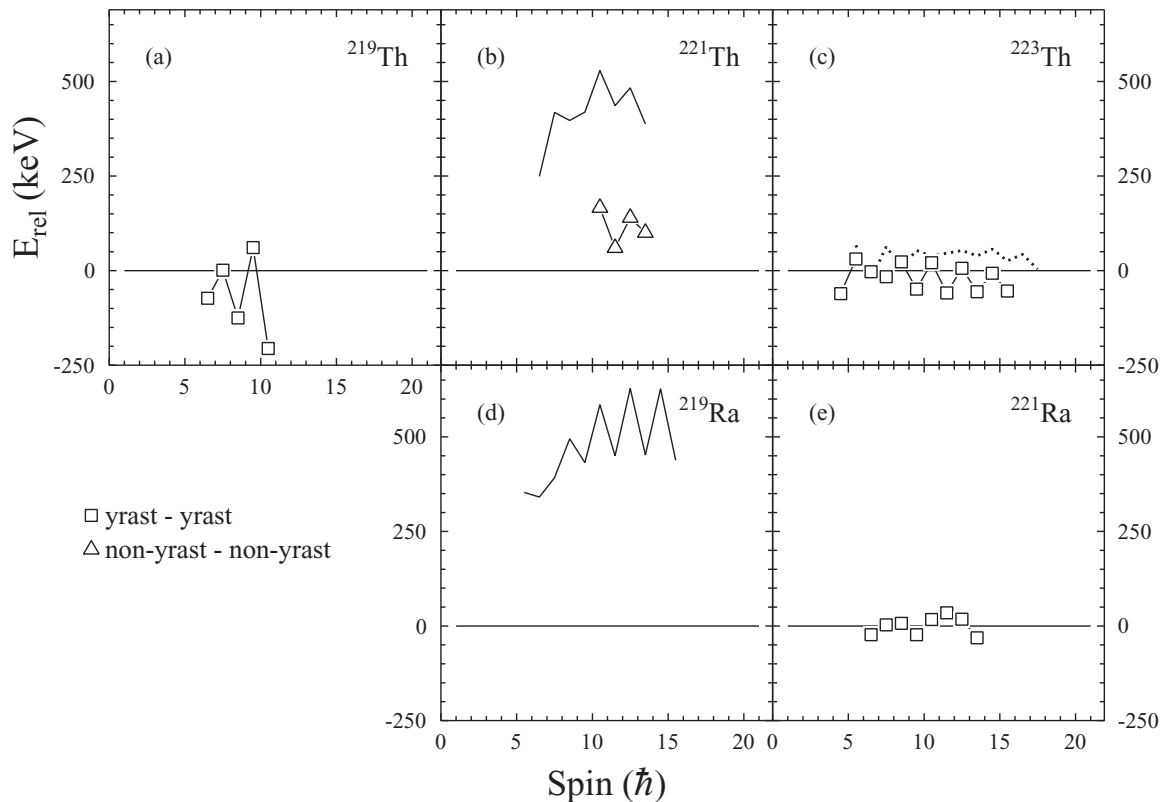


FIG. 15. Relative energies  $E_{\text{rel}} = E(s = +i) - E(s = -i)$  for the odd-mass  $^{219-225}\text{Th}$  nuclei [(a)–(c)] and their respective  $^{219,221}\text{Ra}$  isotones [(d) and (e)]. The  $^{221}\text{Th}$  panel (b) shows  $E_{\text{rel}}$  vs spin for both the two non-yrast bands (triangles) and the corresponding set of non-yrast and yrast band (line). The  $^{223}\text{Th}$  panel (c) contains also the  $E_{\text{rel}}$  function for  $^{225}\text{Th}$ , shown as a dotted line. Only the ground-state bands in  $^{221}\text{Th}$  and  $^{219}\text{Ra}$  are  $K = 1/2$  structures. Note that  $^{217}\text{Ra}$  has no multiple octupole-type structures, while the  $^{223}\text{Ra}$  level scheme is inconclusive in this respect.

$n_{\Omega} = 12$  both emanating from the spherical  $2g_{9/2}$  orbital, and  $\Omega = 1/2, n_{\Omega} = 24$  of  $1i_{11/2}$  parentage. The  $\Omega$  quantum number is useful here despite the fact that the states are often only weakly deformed. In the following, the configuration assignments are simplified, by indicating the occupation of the spherical orbitals by neutrons, although configurations of deformed quasiparticles are used in the calculations.

As seen in Fig. 4 of Ref. [32] and Fig. 1 of Ref. [33], the orbitals  $1i_{11/2}$ ,  $\Omega = 1/2$  and  $2g_{9/2}$ ,  $\Omega = 3/2$  drive the quadrupole deformation strongly in the prolate direction with about the same strength, whereas the  $2g_{9/2}$ ,  $\Omega = 5/2$  orbital is much less shape driving. To obtain configuration assignments, the reader is referred to Table 6 of Ref. [33], where the calculated energies and deformations for the lowest-lying configurations are listed (see also Table III). The onset of quadrupole collectivity in the yrast sequences is qualitatively understood as follows. For the  $N = 129$  isotope  $^{219}\text{Th}$ , the configuration  $(2g_{9/2})^3$ ,  $K = 3/2$  has been proposed [6]. As seen in Fig. 18(c), the quadrupole collectivity is weak. For  $N = 130$ , the configuration is  $(2g_{9/2})^4$ , which has weak quadrupole collectivity as well. The increase is marginal because, due to pairing correlations, the two  $2g_{9/2}$ ,  $\Omega = \pm 3/2$  orbitals are only partially occupied. For  $N = 131$ , the  $1i_{11/2}(2g_{9/2})^4$ ,  $K = 1/2$  configuration is assigned. The occupation of the deformation-driving  $1i_{11/2}$ ,  $\Omega = 1/2$  orbital tips the balance: the  $I(\omega)$  curves for  $^{219}\text{Ra}$  and  $^{221}\text{Th}$  (Fig. 16) indicate a

substantial increase in quadrupole collectivity. For  $N = 132$ , the configuration is  $(1i_{11/2})^2(2g_{9/2})^4$ . Figure 16 demonstrates only a slight increase in quadrupole collectivity through the higher values of  $I(\omega)$  for the  $N = 132$  reference curve as compared to the  $N = 131$  ones. The  $I(\omega)$  functions of the odd- $N$  isotopes are similar to those of their heavier even- $N$  neighbors. This is a consequence of pair correlations: they reduce the occupation of a pair of  $\pm\Omega$  orbitals such that their deformation drive is not much larger than that of the fully occupied  $+\Omega$  orbital in the odd- $N$  neighbor. Since the deformation increases with  $N$ , the quadrupole collectivity of the odd- $N$  isotope is similar to that of its heavier even- $N$  neighbor.

According to Tables 5 and 6 of Ref. [33] (and Table III), two non-yrast configurations need to be considered for  $N = 131$ :  $(2g_{9/2})^5$ ,  $K = 5/2$  (where the odd quasineutron occupies the  $\Omega = 5/2$  state) and  $(1i_{11/2})^2(2g_{9/2})^3$ ,  $K = 3/2$  (with an  $\Omega = 3/2$  quasineutron). The former configuration is expected to lead to smaller quadrupole collectivity than the  $1i_{11/2}(2g_{9/2})^4$ ,  $K = 1/2$  yrast configuration as the strongly deformation-driving  $1i_{11/2}$ ,  $\Omega = 1/2$  orbital is replaced by the weakly-driving  $\Omega = 5/2$ ,  $2g_{9/2}$  one. The  $(1i_{11/2})^2(2g_{9/2})^3$ ,  $K = 3/2$  configuration differs from the  $1i_{11/2}(2g_{9/2})^4$ ,  $K = 1/2$  yrast one by replacing the  $2g_{9/2}$ ,  $\Omega = -3/2$  orbital with the  $2g_{9/2}$ ,  $\Omega = -1/2$  state. Both orbitals are strongly deformation driving. A decrease of quadrupole collectivity can be expected

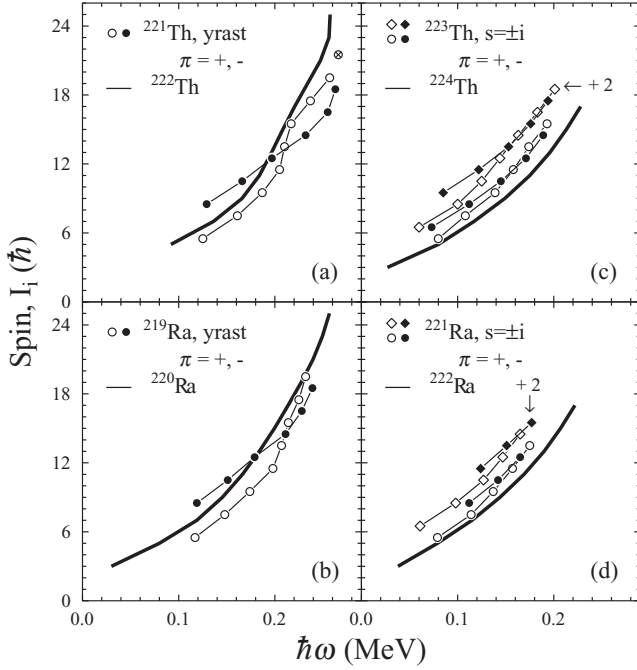


FIG. 16. Spin vs  $\hbar\omega$  for the yrast sequences in  $^{221}\text{Th}$  and  $^{219}\text{Ra}$  [(a) and (b)] and some neighboring odd-mass isotopes,  $^{223}\text{Th}$  and  $^{221}\text{Ra}$  [(c) and (d)]. The positive- and negative-parity states of a simplex-partner band are represented by open and full symbols, respectively. The high-spin extension of the positive-parity states in  $^{221}\text{Th}$  is represented by a cross. The yrast structure of  $^{223}\text{Th}$  and  $^{221}\text{Ra}$  consists of two degenerate sequences with  $s = -i$  and  $s = +i$ . The display of the latter is offset by  $2\hbar$  for clarity. A sequence of the corresponding “reference” even-mass isotope (see text) is shown as a thick line in each case.

as the occupation of the  $2g_{9/2}$  pair, located away from the Fermi level, is larger than that of the  $1i_{11/2}$  pair lying at this level. The calculations of Ref. [33] suggest  $K = 5/2$  and  $K = 3/2$  as the first excited configuration in  $^{221}\text{Th}$  and  $^{219}\text{Ra}$ , respectively. These assignments are supported by the arguments below, based on the measured  $B(E1)/B(E2)$  and  $B(M1)/B(E2)$  ratios.

The  $B(E1)/B(E2)$  ratios are presented as weighted averages over the corresponding spin range, and Table II has been augmented with entries for  $^{219,223,225}\text{Th}$  as well as for  $^{219,221}\text{Ra}$ . The added information is based on evaluating the  $\gamma$ -ray branching ratios and the related transition energies provided in Refs. [12] ( $^{223}\text{Th}$ ), [13] ( $^{225}\text{Th}$ ), [15] ( $^{219}\text{Ra}$ ), and [14] ( $^{221}\text{Ra}$ ). For  $^{219}\text{Th}$ ,  $B(E1)/B(E2)$  ratios were readily available [6]. Like  $^{221}\text{Th}$ ,  $^{219}\text{Ra}$  has yrast and non-yrast octupole structures and a distinction for the  $B(E1)/B(E2)$  ratios has been made accordingly. The data for  $^{219}\text{Ra}$  are given in panel (c) of Fig. 13, and only the error on the average value for the yrast  $B(E1)/B(E2)$  ratios is indicated.

Generally speaking, the  $B(E1)/B(E2)$  ratios in Table II are in line with the benchmark value introduced in Sec. I. However, there are differences between some of these ratios, which allow tests of the predictions of Ref. [33], specifically the configuration-dependent differences in the  $\beta_3$  values. Both quantities can be connected through the simple estimate

TABLE III. Compilation of  $\langle\beta_3\rangle$  values derived from average  $B(E1)/B(E2)$  ratios according to estimate (1) and calculated  $\beta_3$  and  $\beta_2$  values according to Ref. [33]. The nuclei, and their additional labelings in some cases, are the same as in Table II, but  $^{219}\text{Th}$  is omitted. The experimental values are compared with twice the  $\beta_3$  value of the calculations (see text). The  $K$  quantum number represents the assigned configuration (see text). Additional entries for  $^{221}\text{Th}$  and  $^{219}\text{Ra}$  (left partially blank) accommodate additional  $\beta_3$  and  $\beta_2$  values from Ref. [33].

Nucleus	$\overline{B(E1)/B(E2)}$ ( $10^{-6} \text{ fm}^{-2}$ )	$\langle\beta_3\rangle$	$2\beta_3$	$\beta_3$	$\beta_2$	$K$
$^{221}\text{Th}$ (y)	2.17 (24)	0.215 (12)	0.180	0.090	0.101	1/2
$^{221}\text{Th}$ (b, c)	2.28 (37)	0.220 (18)	0.220	0.110	0.094	5/2
$^{221}\text{Th}$				0.083	0.096	3/2 <sup>a</sup>
$^{223}\text{Th}$	1.68 (32)	0.189 (18)	0.212	0.106	0.118	5/2
$^{225}\text{Th}$	0.83 (31)	0.133 (25)	0.216	0.108	0.137	3/2
$^{219}\text{Ra}$ (y)	1.65 (7)	0.188 (4)	0.166	0.083	0.092	1/2
$^{219}\text{Ra}$ (I)	1.07 (28)	0.151 (19)	0.142	0.071	0.088	3/2
$^{219}\text{Ra}$				0.106	0.084	5/2 <sup>a</sup>
$^{221}\text{Ra}$	0.93 (14)	0.141 (10)	0.202	0.101	0.107	5/2

<sup>a</sup>Energetically less favorable according to Ref. [33].

discussed in Ref. [37];

$$\frac{B(E1)}{B(E2)} \simeq 2.694 c_{\text{LD}}^2 A^{2/3} \langle\beta_3^2\rangle \text{ fm}^{-4}. \quad (1)$$

Here,  $c_{\text{LD}} = 6.9 \times 10^{-4} \text{ fm}$  is an appropriate value for the “liquid-drop” constant [37], and the  $\langle\beta_3^2\rangle$  expression represents an average value, independent of spin. As discussed in Refs. [37–39],  $\langle\beta_3\rangle$  values inferred from estimate (1) are typically a factor of 2 larger than the octupole deformations deduced from static mean field calculations, reflecting the fact that the octupole correlations have a strong dynamic component. To arrive at quantitative estimates, the crude assumption is made here that the dynamic part can be taken into account by multiplying the calculated static value by a constant factor of two.

Table III provides, for the nuclei of interest, a compilation of such  $\langle\beta_3\rangle$  values, based on the information in Table II, as well as  $\beta_3$  values calculated for the configurations indicated. The  $^{219}\text{Th}$  nucleus is excluded, in view of the large uncertainty on the  $B(E1)/B(E2)$  ratio. Focussing on the values  $2\beta_3$ , experimental information and theory indicate the following consistent trends for  $^{221}\text{Th}$  and its nearest neighbors: (i) The difference in  $\langle\beta_3\rangle$  between the non-yrast structures of  $^{221}\text{Th}$  and  $^{219}\text{Ra}$  is consistent with a  $K = 5/2$  assignment for the former and a  $K = 3/2$  one for the latter. (ii) The  $\langle\beta_3\rangle$  values for the yrast and non-yrast structures of  $^{221}\text{Th}$  are both reasonably close to the calculated  $2\beta_3$  ones for the  $K = 1/2$  and  $K = 5/2$  configurations, respectively. (iii) The same holds true for  $^{219}\text{Ra}$ , if the suggested  $K = 3/2$  assignment for the non-yrast structure is adopted. (iv) The values  $\langle\beta_3\rangle$  for the yrast sequences of  $^{221}\text{Th}$  and  $^{223}\text{Th}$  are both also reasonably close to the corresponding calculated  $2\beta_3$  ones. In addition, the above assignments for the non-yrast structures of  $^{221}\text{Th}$  and  $^{219}\text{Ra}$  concur with the energetically favored configuration in each case.

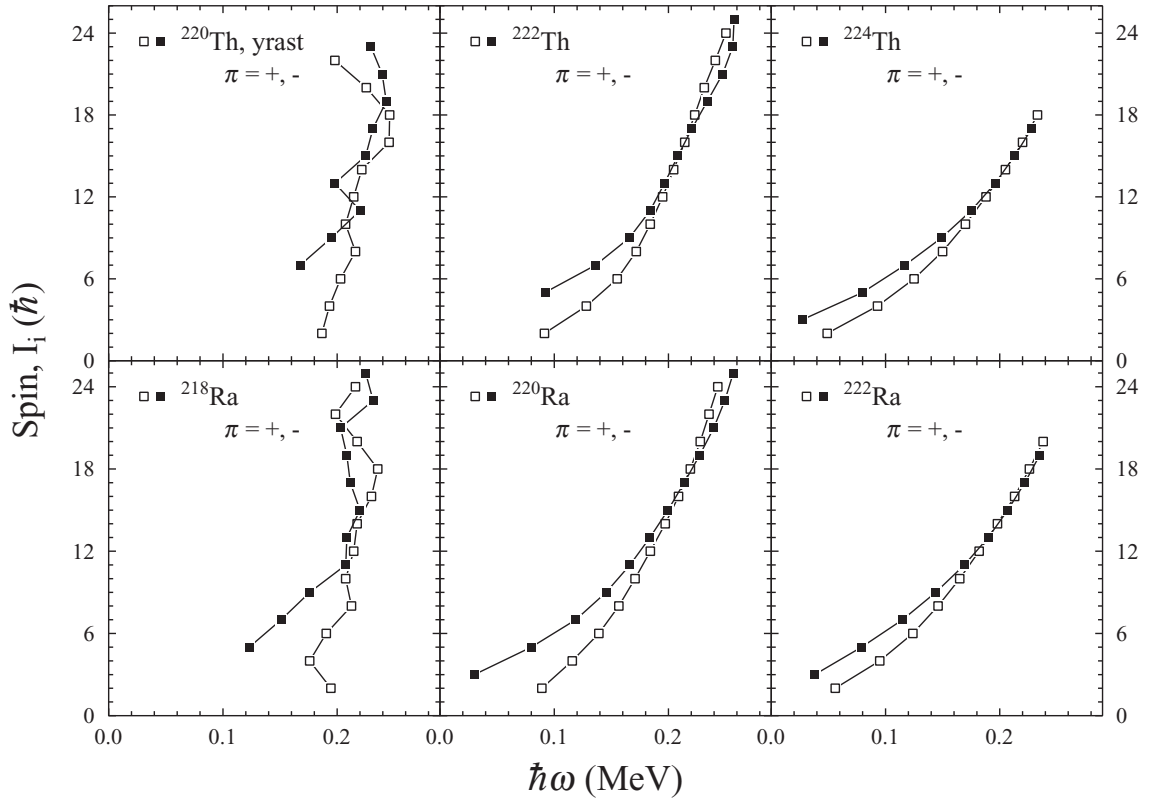


FIG. 17. Spin vs  $\hbar\omega$  for the yrast sequences in the neighboring  $^{220,222,224}\text{Th}$  (top) and  $^{218,220,222}\text{Ra}$  nuclei (bottom). The positive- and negative-parity states of a simplex-partner band are represented by open and full symbols, respectively. The data for  $^{218}\text{Ra}$  and  $^{220}\text{Ra}$  are truncated above spin 25.

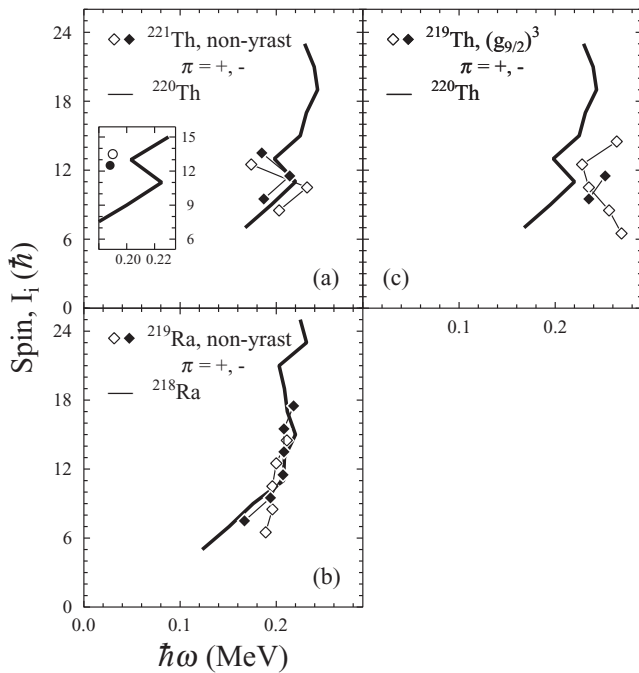


FIG. 18. Similar to Fig. 16, but for the non-yrast sequences in  $^{221}\text{Th}$  (a) and  $^{219}\text{Ra}$  (b) and the yrast  $(g_{9/2})^3$  sequence in  $^{219}\text{Th}$  (c). The two sequences in  $^{221}\text{Th}$  are presented separately in the main panel ( $s = +i$ ) and the inset ( $s = -i$ ) for clarity. The “reference” even-mass isotope is different from Fig. 16 (see text).

For  $^{225}\text{Th}$  and  $^{221}\text{Ra}$ , a disagreement is found between the experimental and theoretical information in Table III. Arguably, this may be due to the rather poor knowledge of the experimental  $B(E1)/B(E2)$  ratios. Nevertheless, a consistent picture emerges for all other nuclei, suggesting that the configuration assignments are reasonable.

As indicated in Fig. 14, the  $B(M1)/B(E2)$  ratios available for  $^{223}\text{Th}$  [12] and  $^{219}\text{Ra}$  [15] can be compared with those for  $^{221}\text{Th}$ . The average value for  $^{223}\text{Th}$  is  $B(M1)/B(E2) = 7.12(252) \times 10^{-6} \mu_N^2/(e^2\text{fm}^4)$ . For  $^{219}\text{Ra}$ , a set of  $M1$  linking transitions for initial spins  $15/2 \leq I \leq 31/2$  are reported [15], but mixing ratios  $\delta$  are not provided in the literature. Here, an estimate  $B(M1)/B(E2) \leq 0.58 \times 10^{-6} \mu_N^2/(e^2\text{fm}^4)$  is used, which represents the upper limit of the average value computed assuming  $\delta = 0$  mixing in each case. Overall, the  $B(M1)/B(E2)$  ratios for  $^{221}\text{Th}$  and  $^{223}\text{Th}$  are close, and comparatively large with respect to the  $^{219}\text{Ra}$  limit.

To evaluate the information on  $B(M1)$  values, the following approach can be taken. Based on the  $\beta_2$  values of Ref. [33], quadrupole moments,  $Q_0$ , are calculated for the configurations under discussion. With these moments,  $B(E2)$  probabilities are computed for a given  $I$  and  $K$  value of the configuration, using the corresponding Clebsch-Gordan coefficient (the value of  $K$  does not change since the  $E2$  transition is an “intra-band” one). Finally,  $B(M1)$  values are obtained from the  $B(M1)/B(E2)$  ratios. This approach depends on the assumption of  $Q_0$  being independent of spin. Despite this limitation, the  $B(M1)$  probabilities obtained in this way can provide guidance for

TABLE IV. Estimates of  $B(M1)$  values for  $^{221,223}\text{Th}$  and  $^{219}\text{Ra}$  based on the data of Fig. 14 and the calculated  $\beta_2$  values of Ref. [33]. The set of  $\overline{B(M1)}$  values should be taken as a guide to distinguish between the different configurations under discussion.

Nucleus	$\beta_2$	$Q_0$ (efm <sup>2</sup> )	$K$	Spins (parities) or spin range	$\overline{B(M1)}$ ( $10^{-2}\mu_N^2$ )
$^{221}\text{Th}$ (b, c)	0.094	337.1	5/2	$I^\pi = 19/2^-, 23/2^-$	1.19 (21)
$^{223}\text{Th}$	0.118	425.7	5/2	$I^\pi = 9/2^+, 11/2^+$	2.03 (70)
$^{219}\text{Ra}$ (I)	0.088	306.7	3/2	$15/2 \leq I \leq 31/2^a$	$\leq 0.17^b$

<sup>a</sup>All states have negative parity.

<sup>b</sup>Estimate assuming  $\delta = 0$ .

configuration assignments, especially when these values differ from each other.

Table IV summarizes the steps of the present approach. The results are reported as weighted-average  $\overline{B(M1)}$  values determined, in each case, from the  $B(M1)$  probability for the spins listed. The  $\overline{B(M1)}$  estimates for  $^{221}\text{Th}$  and  $^{223}\text{Th}$  are similar, but are markedly larger than the corresponding value for  $^{219}\text{Ra}$ . These findings are consistent with the suggested difference in the  $K$  quantum number.

Lastly, the comparison between panels (a) and (c) of Fig. 18, where the alignment plots for the non-yrast structures of  $^{221}\text{Th}$  deviate from the corresponding trajectories of  $^{219}\text{Th}$ , leads to disfavoring a  $K = 3/2$ ,  $(1i_{11/2})^2(2g_{9/2})^3$  assignment. This observation also supports the proposed  $K = 5/2$  configuration.

Another issue originating from the comparison with neighboring nuclei deserves attention: the energy splitting between

states of opposite parity in a sequence of a given simplex. The parity splitting as a function of spin, expressed as

$$\delta E(I^-) = E(I^-) - \frac{(I+1)E_{(I-1)^+} + IE_{(I+1)^+}}{2I+1}, \quad (2)$$

is a measure of the degree of static octupole deformation. Figure 19 indicates that, in the mass region under discussion,  $\delta E$  has typically a large positive value at low spin, then changes sign, and tends toward 0 at the highest spins.

The  $\delta E \sim 0$  values at high spin indicate that rotation stabilizes octupole deformation. The detailed mechanism has been discussed in Ref. [10], where it is noted that “The conventional interpretation in terms of a pear shape and tunneling does not account for these observations in a simple way. It suggests the alternative interpretation of condensation of rotational-aligned octupole phonons.” Specifically, along the yrast sequence, subsequent alignments of octupole phonons with the rotational axis compete with the increase in rotational frequency of the quadrupole-deformed nucleus. With respect to Fig. 19, the scenario is as follows. First, the  $\pi = -$  state with one aligned octupole phonon crosses the  $\pi = +$  zero-phonon state because it is energetically favored. At the crossing,  $\delta E$  becomes negative. Subsequently, the  $\pi = +$  two-phonon state crosses the zero-phonon one. The two states repel each other as they have the same parity and mix. This “avoided” crossing is seen as the upbend of  $\delta E$  in Fig. 19. Figure 17 illustrates the successive alignment of the octupole phonons. For example, in  $^{220}\text{Ra}$  and  $^{222}\text{Th}$  around  $\hbar\omega = 0.1$  MeV, the  $\pi = -$  sequence has  $3\hbar$  of angular momentum more than the  $\pi = +$  sequence, indicative of an aligned octupole phonon. The alignment

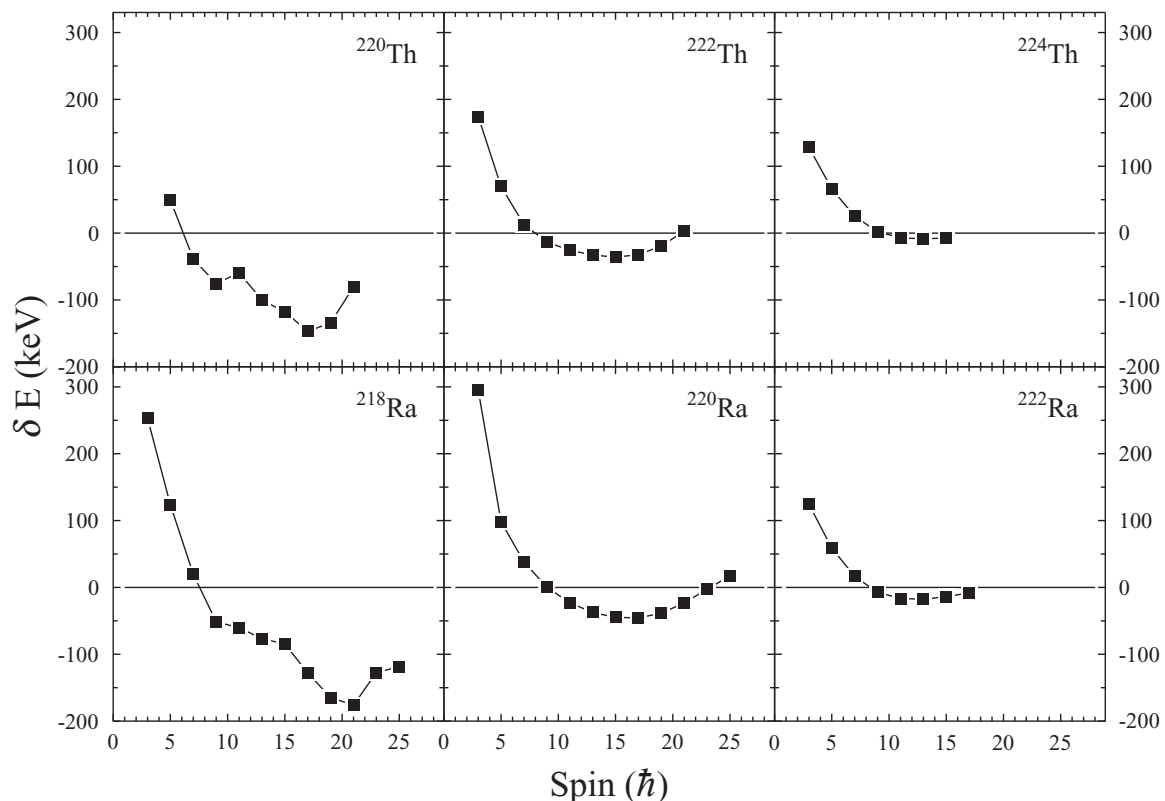


FIG. 19. Parity splitting,  $\delta E$ , as a function of the spin for the yrast sequences in  $^{220,222,224}\text{Th}$  (top) and  $^{218,220,222}\text{Ra}$  (bottom).

difference between the negative- and positive-parity sequences,  $I_-(\omega) - I_+(\omega)$ , decreases when the zero-phonon state mixes with the two-phonon one, with the latter sequence carrying  $6\hbar$ . At the center of the “avoided” crossing, where the mixing is equal, the octupole phonons contribute  $3\hbar$  to the total angular momentum of the  $\pi = +$  sequence, and the same amount to the  $\pi = -$  one. The functions  $I_{\pm}(\omega)$  of the two parities agree, and the function  $\delta E$  has a minimum, because its derivative is equal to  $I_+(\omega) - I_-(\omega)$ . At larger  $\omega$  values, the  $\pi = +$  sequence attains progressively two-phonon character, while the  $\pi = -$  sequence still retains its one-phonon structure. Accordingly,  $I_+ > I_-$ , and  $\delta E$  increases with  $I$ . Around  $\hbar\omega = 0.24$  MeV, the  $\pi = +$  sequence has mostly two-phonon character and  $I_+ - I_- \approx 3\hbar$ . At the highest frequencies, the  $I_{\pm}(\omega)$  functions come again closer, as the three-phonon state begins to mix into the  $\pi = -$  sequence. This dynamic scenario is related to the one of a static octupole deformation, since the mixing of the zero- and two-phonon states is associated with a finite expectation value of the octupole operator that is of the order of the calculated static octupole moments. As stated in Sec. I,  $K$  is not necessarily a good quantum number. It is used here to indicate whether there is an angular-momentum component within the reflection plane, which generates parity doublets. In the absence of such a component, a single rotational sequence of a given simplex is present. Moreover, using  $K$  allows one to relate in a simple way to previous work, which assumed axial shape.

The  $\delta E$  vs  $I$  behavior for  $^{221}\text{Th}$  and neighboring odd-mass nuclei is presented in Fig. 20. The panels (a) and (b) for the  $^{221}\text{Th}$  and  $^{219}\text{Ra}$  isotones give the combination of yrast and non-yrast bands, while the panels (c) and (d) for the heavier odd-mass isotones contain only information from yrast states. Figures 16 and 20 suggest that the scenario of rotation-induced condensation of octupole phonons is also applicable to the yrast sequences of  $^{221}\text{Th}$  and  $^{219}\text{Ra}$ , which are based on  $K = 1/2$  configurations. By comparison with Fig. 19, the parity splitting is, at low spin, smaller than in both even- $N$  neighbors and the minimum of  $\delta E$  is lower than in the heavier neighbor, but higher than in the lighter one. The  $I_- - I_+$  value is  $\approx 3\hbar$ , far below the “avoided” crossing for both isotopes, and becomes  $-3\hbar$  above the latter. In the case of  $^{221}\text{Th}$ , the last point of the  $\pi = -$  sequence shows an increase of  $I_-$  which is likely caused by the admixture of the three-phonon state.

As discussed above, the functions  $I(\omega)$  of the  $K \geq 3/2$  non-yrast sequences are similar to the ones in the lighter neighbor. The parity splittings are rather different from those of the neighbors, shown on the right side of Fig. 20, but no clear trend is recognizable. The plots on the left side, on the other hand, demonstrate that there are distinct differences in  $\delta E$ , not only between the yrast and non-yrast bands in a given nucleus, but also between the non-yrast bands in  $^{221}\text{Th}$  and  $^{219}\text{Ra}$ . This supports the conclusion above that the non-yrast bands in these two nuclei are based on different configurations.

For  $N = 132$ , the plots in Fig. 17 indicate that the alignment difference  $I_- - I_+$  is only about  $2\hbar$  at low spin and goes to zero at high spin. Correspondingly, the parity splitting starts at a smaller  $\delta E$  value and barely assumes negative values. This reflects the trend toward more static octupole and larger quadrupole deformation as  $N$  increases. Within

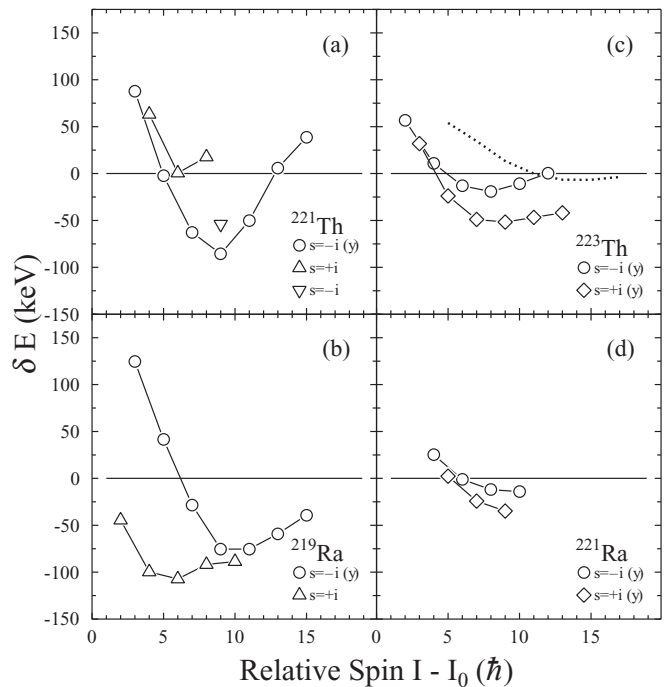


FIG. 20. Parity splitting as a function of the spin above the ground state,  $(I - I_0)$ , for  $^{221}\text{Th}$  (a),  $^{219}\text{Ra}$  (b),  $^{223}\text{Th}$  (c), and  $^{221}\text{Ra}$  (d). The yrast structures are labeled by “y”. The  $\delta E$  function for  $^{225}\text{Th}$  is included in panel (c) and only the  $s = -i$  structure is shown (dotted line) as it is representative of both simplex sequences of the yrast structure.

the octupole-phonon-condensation picture, this is attributed to the combination of a low-frequency, smooth admixture of the two-phonon state into the  $\pi = +$  sequence and an increased resistance against the alignment of the octupole phonon with the rotational axis due to the larger quadrupole deformation. The plots for the  $^{223}\text{Th}$ – $^{221}\text{Ra}$  pair indicate that the parity-doublet bands reflect the same trend in a somewhat enhanced manner. Figure 16 shows that, at low spin, the  $s = +i$  partner of the parity doublet in  $^{223}\text{Th}$  has  $I_- - I_+ \approx 2\hbar$  and the  $s = -i$  partner only  $I_- - I_+ \approx 1\hbar$ . The parity splittings in panels (c) and (d) of Fig. 20 exhibit the trend, with the  $s = -i$  sequence having less parity splitting than the  $s = +i$  one. Although less comprehensive, the  $^{221}\text{Ra}$  data are consistent with this picture. The trend continues in the case of  $^{225}\text{Th}$ . Here, the parity splittings in both simplex sequences are particularly close, and only a single simplex structure is shown.

At low spin, the parity splittings in the odd- $N$  nuclei are systematically smaller than those in their even- $N$  neighbors, while at higher spin, the  $\delta E$  values are quite comparable. One may speculate that this is a consequence of pairing correlations, which increase the excitation energy of the octupole phonons and reduce their coupling to the quadrupole deformed nucleus. At low spin, neutron pairing is strong in the even- $N$  nuclei, but reduced in the odd- $N$  ones due to blocking. As a consequence, the excitation energy of the octupole phonon is reduced (smaller  $\delta E$ ). At high spin, neutron pairing is quenched and there is no systematic difference between even- and odd- $N$  nuclei. This picture is consistent with a reduction of the

parity splitting in configurations with a substantial  $K$  value, as compared to the ones with  $K \approx 0$ , as noticed in Refs. [1,11].

A comment on the end point of the yrast octupole band in  $^{221}\text{Th}$  at  $39/2^+$  is in order. As seen in the inset of Fig. 12, the intensity drops and evidence is lacking for the anticipated next  $E1$  transition, feeding the  $39/2^+$  level. As shown in Fig. 16, the corresponding rotational frequency is  $\hbar\omega \sim 0.26$  MeV at this point. This frequency is close to the  $\hbar\omega \sim 0.25$  MeV value at which a sudden drop in intensity was found in the octupole band of  $^{222}\text{Th}$ , with corresponding spins of  $24^+$  and  $25^-$  [18]. Thus, the observations in both nuclei are similar. As discussed above, the location in frequency and spin of the highest states in  $^{221}\text{Th}$  and  $^{222}\text{Th}$  is consistent with the interpretation in terms of the condensation of octupole phonons. However, the change in the feeding pattern may indicate the presence of additional configurations which are, beyond 0.26 MeV, energetically favored over the octupole band. Theory predicts for  $^{222}\text{Th}$  that, at the same frequency, a transition from an octupole to a reflection-symmetric shape occurs, induced by a rotation-aligned  $i_{13/2}$  proton pair and, perhaps, a  $j_{15/2}$  neutron pair [17]. It is possible that a similar interpretation holds for  $^{221}\text{Th}$ , and the  $(43/2^+)$  state might then indicate the anticipated structural change.

## V. CONCLUSIONS

Multiple octupole-type band structures have been observed and characterized in  $^{221}\text{Th}$ . The main feature of the level scheme is the presence of two, high-lying band structures in addition to the  $K = 1/2$  yrast octupole band. Higher-lying excitations are present as well, but these do not form band structures. The high-lying octupole bands exhibit features

of energetically nearly degenerate parity-doublet sequences. They are proposed to be associated with the  $K = 5/2$  configuration that is associated with the yrast structure of  $^{223}\text{Th}$ . The observation of this set of level sequences in  $^{221}\text{Th}$  completes the systematics of parity-doublet bands in the mass region. From comparisons of level structures in the Th and Ra isotopic chains, a grouping of the  $K = 0$  and the  $K = 1/2$  bands of even-even and odd-mass nuclei, respectively, as structures with good simplex quantum number and no parity doublets emerges. In the  $K \geq 3/2$  bands, on the other hand, the simplex symmetry is broken and degeneracy occurs. The two high-lying band structures in  $^{221}\text{Th}$  resemble the vibrational-like behavior seen in the lighter isotopes, in particular in  $^{220}\text{Th}$ . Thus, just as was the case for the band structures in the latter isotope, the high-lying sequences in  $^{221}\text{Th}$  may be called “tidal” bands, referring to the tidal-wave picture for octupole nuclei discussed in Refs. [7,8]. In contrast, the yrast band behaves in a more rotational-like fashion and approaches the behavior seen in the heavier isotopes. The interpretation of the  $\pi = \pm$  yrast sequences in even-even nuclei as rotation-induced condensation of octupole phonons [10] carries over to the odd- $N$  nuclei, where the presence of the odd neutron seems to reduce fluctuations in the octupole degree of freedom.

## ACKNOWLEDGMENTS

The authors thank J. Elson (WU) and J. Rohrer (ANL) for technical support and J. P. Greene (ANL) for the preparation of the targets. This work was supported by the US Department of Energy, Office of Nuclear Physics, Contracts No. DE-FG02-88ER-40406, No. DE-AC02-06CH11357, No. DE-FG02-95ER40934, and No. DE-FG02-94ER40834, and by the National Science Foundation, Grant No. PHY-0854815.

- 
- [1] P. A. Butler and W. Nazarewicz, *Rev. Mod. Phys.* **68**, 349 (1996), and references therein.
- [2] I. Wiedenhöver *et al.*, *Phys. Rev. Lett.* **83**, 2143 (1999).
- [3] X. Wang *et al.*, *Phys. Rev. Lett.* **102**, 122501 (2009).
- [4] D. Ward *et al.*, *Nucl. Phys. A* **600**, 88 (1996).
- [5] S. Zhu *et al.*, *Phys. Rev. C* **81**, 041306 (2010).
- [6] W. Reviol *et al.*, *Phys. Rev. C* **80**, 011304(R) (2009).
- [7] W. Reviol *et al.*, *Phys. Rev. C* **74**, 044305 (2006).
- [8] W. Reviol *et al.*, *Acta Phys. Pol. B* **42**, 671 (2011).
- [9] Additional details may be found in S. Frauendorf, Y. Gu, and J. Sun, *Int. J. Mod. Phys. E* **20**, 465 (2011).
- [10] S. Frauendorf, *Phys. Rev. C* **77**, 021304(R) (2008).
- [11] S. G. Frauendorf, *Rev. Mod. Phys.* **73**, 463 (2001).
- [12] M. Dahlinger, E. Kankleit, D. Habs, D. Schwalm, B. Schwartz, R. S. Simon, J. D. Burrows, and P. A. Butler, *Nucl. Phys. A* **484**, 337 (1988).
- [13] J. R. Hughes *et al.*, *Nucl. Phys. A* **512**, 275 (1990).
- [14] F. Fernandez-Niello, C. Mittag, F. Riess, E. Ruchowska, and M. Stalknecht, *Nucl. Phys. A* **531**, 164 (1991).
- [15] M. Wieland *et al.*, *Phys. Rev. C* **45**, 1035 (1992).
- [16] The case of  $^{227}\text{Th}$ , discussed in N. J. Hammond *et al.*, *Phys. Rev. C* **65**, 064315 (2002), is not considered here; the  $s = \pm i$  structures are displaced in energy ( $-590 \leq E_{rel} \leq -235$  keV, cf. Fig. 15).
- [17] W. Nazarewicz, G. A. Leander, and J. Dudek, *Nucl. Phys. A* **467**, 437 (1987).
- [18] J. F. Smith *et al.*, *Phys. Rev. Lett.* **75**, 1050 (1995).
- [19] I. Y. Lee, *Nucl. Phys. A* **520**, 641c (1990).
- [20] W. Reviol, D. G. Sarantites, R. J. Charity, C. J. Chiara, J. Elson, M. Montero, O. L. Pechenaya, S. K. Ryu, and L. G. Sobotka, *Nucl. Instrum. Methods A* **541**, 478 (2005).
- [21] <http://ns12.anl.gov/pdfs/Reviol.pdf>.
- [22] S. K. Tandel *et al.*, *Phys. Rev. C* **87**, 034319 (2013).
- [23] N. I. Ashwood *et al.*, *J. Phys. G* **32**, 463 (2006).
- [24] D. C. Radford, *Nucl. Inst. Meth. A* **361**, 297 (1995).
- [25] R. K. Sheline, C. F. Liang, P. Paris, A. Gizon, and V. Barci, *Phys. Rev. C* **49**, 725 (1994).
- [26] NNDC database, <http://www.nndc.bnl.gov/nudat2>.
- [27] P. Kuusiniemi *et al.*, *Acta Phys. Pol. B* **32**, 1009 (2001).
- [28] Here,  $A_4/A_0 > 0$  is a consequence of an  $E2$  admixture ( $A_4 > 0$ ). Examining expression (7) and Table II b in T. Yamazaki, *Nucl. Data Tables A* **3**, 1 (1967), for  $k = 4$ , one finds that only the  $\delta^2$  term ( $\delta$  being the  $E2/M1$  mixing ratio) has a nonzero  $f_4$  coefficient. For example, for a  $19/2 \rightarrow 17/2$  mixed transition,  $f_4 = 0, 0$ , and  $0.534$  for angular momenta  $L_1L_1, L_1L_2$ , and  $L_2L_2$ , respectively, and, thus,  $A_4 > 0$ .
- [29] N. Schulz *et al.*, *Phys. Rev. Lett.* **63**, 2645 (1989).
- [30] F. Cristancho *et al.*, *Phys. Rev. C* **49**, 663 (1994).

- [31] <http://bricc.anu.edu.au/index.php>.
- [32] G. A. Leander and Y. S. Chen, *Phys. Rev. C* **37**, 2744 (1988).
- [33] S. Cwiok and W. Nazarewicz, *Nucl. Phys. A* **529**, 95 (1991).
- [34] L. Riley *et al.*, *Phys. Rev. C* **62**, 021301(R) (2000).
- [35] B. Ackermann *et al.*, *Nucl. Phys. A* **559**, 61 (1993).
- [36] J. F. C. Cocks *et al.*, *Phys. Rev. Lett.* **78**, 2920 (1997).
- [37] W. Nazarewicz and P. Olanders, *Nucl. Phys. A* **441**, 420 (1985).
- [38] D. Ward, G. D. Dracoulis, J. R. Leigh, R. J. Charity, D. J. Hinde, and J. O. Newton, *Nucl. Phys. A* **406**, 591 (1983).
- [39] G. A. Leander, W. Nazarewicz, G. F. Bertsch, and J. Dudek, *Nucl. Phys. A* **453**, 58 (1986).